Automated Design Architectures for Co-orbiting Spacecraft Swarms for Planetary Moon Mapping

Ravi teja Nallapu, Jekan Thangavelautham*

Space and Terrestrial Robotic Exploration (SpaceTREx) Laboratory, Asteroid Science, Technology and Exploration Research Organized by Inclusive eDucation (ASTEROID) Laboratory, Department of Aerospace and Mechanical Engineering, The University of Arizona, 1130 N Mountain Ave, Tucson, AZ, USA, 85721

Abstract

This work describes the design and optimization of spacecraft swarm missions to meet spatial and temporal visual mapping requirements of missions to planetary moons, using resonant co-orbits. The algorithms described here are a part of Integrated Design Engineering and Automation of Swarms (IDEAS), a spacecraft swarm mission design software that automates the design trajectories, swarm, and spacecraft behaviors in the mission. In the current work, we focus on the swarm design and optimization features of IDEAS, while showing the interaction between the different design modules. In the design segment, we consider the coverage requirements of two general planetary moon mapping missions: global surface mapping and region of interest observation. The configuration of the swarm co-orbits for the two missions is described, where the participating spacecraft have resonant encounters with the moon on their orbital apoapsis. We relate the swarm design to trajectory design through the orbit insertion maneuver performed on the interplanetary trajectory using aero-braking. We then present algorithms to model visual coverage, and collision avoidance in the swarm. To demonstrate the interaction between different design modules, we relate the trajectory and swarm to spacecraft design through fuel mass, and mission cost estimations using preliminary models. In the optimization segment, we formulate the trajectory and swarm design optimizations for the two missions as Mixed Integer Nonlinear Programming (MINLP) problems. In the current work, we use Genetic Algorithm as the primary optimization solver. However, we also use the Particle Swarm Optimizer to compare the optimizer performance. Finally, the algorithms described here are demonstrated through numerical case studies, where the two visual mapping missions are designed to explore the Martian moon Deimos.

Keywords: Spacecraft Swarms, Automated Mission design, Planetary Moon

*Corresponding author

Email addresses: rnallapu@email.arizona.edu (Ravi teja Nallapu), jekan@arizona.edu (Jekan Thangavelautham)

Exploration, Resonant Co-orbits, Evolutionary optimization algorithms

1. Introduction

Planetary moon exploration sheds fundamental insight into topics such as solar system origin, and astrobiology. Specifically, the in situ exploration of small irregular moons are being pursued to study the formation of planets and search for extraterrestrial habitats (Castillo-Rogez, Pavone, Hoffman, et al., 2012). Additionally, several technologies for in situ exploration of these moons are being developed (Nallapu, Thoesen, Garvie, et al., 2016). However, the uncertainties in the knowledge of surface properties can be challenging for in situ missions without prior reconnaissance (Balázs, 2018). However, small planetary moons, such as the Martian moons, have small spheres of influence (Wallace, Parker, Strange, et al., 2012), suggesting that it is virtually impossible to perform reconnaissance from Keplerian orbits around them. (Zamaro and Biggs, 2016), leaving flybys as a viable option. In this work, we focus on visual mapping reconnaissance, which faces two important challenges: firstly, at a given time, nearly 50 % of the moon is shadowed from Sunlight, and secondly, most planetary moons are tidally locked uniform rotators (Aleshkina, 2009), which limits the surface coverage at a fixed encounter location. Clearly, single spacecraft flybys suffer from spatial and temporal coverage limitations, suggesting that multi-spacecraft missions are efficient alternatives. However, the design of a swarm mission adds additional layers of difficulty to the multi-disciplinary spacecraft mission design (Wertz, Everett, and Puschell, 2011). Especially, during the initial mission planning phase where several decisions are free variables, an automated architecture that provides optimal mission concepts will accelerate the design process (Wertz, Everett, and Puschell, 2011). To provide such an automated platform, we proposed the Integrated Design Engineering and Automation of Swarms (IDEAS) software in Nallapu and Thangavelautham (2019a). The IDEAS architecture divides a swarm mission design into three individual optimization problems: trajectory, swarm, and spacecraft optimization. The architecture of the IDEAS software is presented in Figure 1. As shown here, the three individual modules: Automated Trajectory Designer, Automated Swarm Designer, and Automated Spacecraft Designer modules will form the Mission Solver module where the three design processes are automated. The design modules receive high-level inputs such as objectives, constraints, and mission parameters through a user interface. The IDEAS is developed in the MATLAB programming environment because of its inbuilt state-of-the-art numerical propagators and optimizers (Hanselman and Littlefield, 2005). In this work, each broad qualitative decision (such as the use of aerobraking, and use of co-orbits) is referred to as behavior which results in a different set of design variables. An inventory of such behaviors is maintained in the Knowledge Base module of IDEAS. The Knowledge Generator module is used for populating these behavior inventories. Additionally, space mission design is an iterative process (Wertz, Everett, and Puschell, 2011). For this reason, IDEAS will have

a Mission Analyzer module that checks if the design requirements are satisfied. A key advantage of such a unifying architecture is that it reduces the scope for bottlenecks such as duplication, and incompatibility of different designed systems.

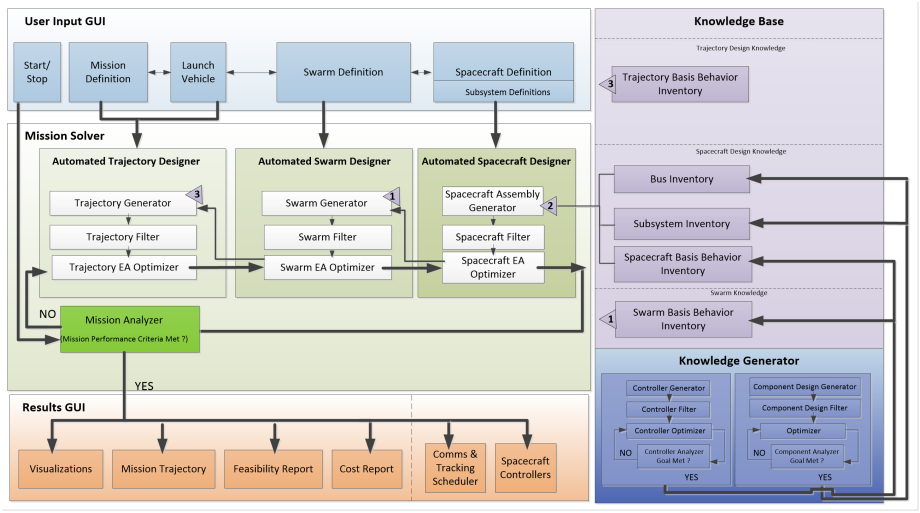

Figure 1: Software architecture of the proposed IDEAS software to provide an end-to-end design framework for spacecraft swarm missions.

In this work, we use the Automated Swarm Designer module to design spacecraft swarms that meet spatial and temporal requirements on visual mapping missions to planetary moons. The swarm will be deployed on resonant co-orbits, which have periodic flybys the moon on their apoapsis. Two types of visual mapping missions are considered in the current work: i) global surface mapping, ii) region of interest (RoI) observation. The global surface mapping mission focuses on spatial coverage, while the RoI observation mission mainly focuses on the temporal coverage requirements. While the focus of the current work is on the swarm designer module, we demonstrate the interaction between different design modules by designing the interplanetary trajectory, and preliminary design of spacecraft in the swarm. We begin by presenting the requirements of the two missions. Noting that their coverage requirements are different, two different configurations of the swarm are presented. Both configurations involve encounters with the target moon at a specified orbital location when the spacecraft are located on their apoapsis. We then relate the swarm design with the trajectory design problem through their orbit insertion maneuvers. We assume that the swarm uses aerobraking (Vallado, 2013) at the central planet hosting the moon, to enter into these co-orbits. The orbit insertion maneuver will be split into two components: a planar capture that requires a tangential impulsive maneuver on the periapsis of the arrival hyperbola, and an orientation change of the arrival hyperbola to facilitate a moon encounter at the specified

orbital location. This allows us to constrain the orbital elements of the co-orbits, such that the total orbit insertion fuel requirements are upper-bounded. We then present algorithms to model coverage and collision avoidance among the swarms. Following this, we relate the two problems to the spacecraft design, by estimating the fuel mass, and mission costs through preliminary estimating relations. We then formulate the trajectory and swarm optimization problems of the two missions as mixed-integer nonlinear programming (MINLP) problems which are solved using two evolutionary optimization algorithms (Rao, 2019). For simplicity, we maintain the same trajectory design problem for both missions. A genetic algorithm (GA) solver (Conn, A. Perez, Plice, et al., 2017) is used as the primary optimization solver, however we use the particle swarm optimizer(PSO) algorithm (Kennedy and Eberhart, 1995) using penalty functions (Rao, 2019) in-order to compare the optimizer performance. Finally, we develop numerical case studies of the two visual mapping missions, by designing swarm missions to explore the Martian moon Deimos using the IDEAS architecture. The optimal trajectory and swarm designs are noted and their performance is examined. A seed spacecraft with dry mass populated using commercially available off-the-shelf small spacecraft hardware is used, with fuel requirements and costs computed using the maneuver requirements of the trajectory and swarm design. The organization of this work is as follows. Section 2 presents related work done on planetary moon exploration, and swarm missions. Section 3 presents the modeling methodology used in the current work. Here we present the models to configure the resonant co-orbits of the swarm for the two missions. The constraints on the classical orbital elements (COEs) of the co-orbits from the spacecraft camera and the interplanetary trajectory are presented, along with algorithms to model the surface coverage of the moon, collision avoidance, and mission costs. These models are used in Section 4 to formulate the MINLP problems corresponding to the trajectory and swarm design problems of the two missions. The optimization solvers and their implementation are also described here. In section 5 we present the results of case studies where the two visual mapping missions to explore Deimos are designed. The dry mass of the seed spacecraft is described in Appendix A. Finally, Section 6 summarizes the key contributions of the current work and identifies pathways forward for the development of IDEAS.

2. Related Work

Co-orbital exploration has been a major source of planetary moon exploration. For instance, the exploration of Martian moons has been largely done from co-orbital observations of Martian orbiting spacecraft (Duxbury, Zakharov, Hoffmann, et al., 2014). Resonant Co-orbits were studied as viable trajectories to explore Europa (Buffington, 2014). In the near future, dedicated missions to planetary moons such as the MMX (Campagnola, Yam, Tsuda, et al., 2018), JUICE (Grasset, Dougherty, Coustenis, et al., 2013), and Europa Clipper mission (C. B. Phillips and Pappalardo, 2014) have been planned. Existing work

on co-orbit design focused on the derivation of orbital elements assuming equatorial and circular moon orbits (Conte, 2014). Coverage modeling, on these co-orbits, is a critical aspect of the current work. Most coverage evaluation algorithms assume a spherical target and a circular sensor (Wertz, Everett, and Puschell, 2011). Camera transforms, on the other hand, provide a faster method to model the coverage of irregular shapes, inside the field of view (FoV) of a square sensor (Sobel, 1972). In the current work, we use camera transforms to model the instantaneous coverage of the spacecraft swarms. Traditionally, swarm missions have been classified into 2 types: formation flying and constellations (Bandyopadhyay, Foust, Subramanian, et al., 2016). However, recognizing that multi-spacecraft missions can be designed with a wide variety of interactions, we broadly classify spacecraft swarm architectures into 5 classes as described in Nallapu and Thangavelautham (2019c):

1. Class 0 Swarms: This is simply a collection of multiple spacecraft that exhibit no coordination either in movement, sensing, or communication.
2. Class 1 Swarms: Each spacecraft coordinates its movement resulting in formation flying but there is no explicit communication coordination or sensing coordination.
3. Class 2 Swarms: Each spacecraft coordinates movement and communication including using Multiple-Input-Multiple-Output (MIMO) or parallel channels. The swarm has collective sensing capabilities but is not optimized with respect to the swarm.
4. Class 3 Swarms: Each spacecraft coordinates sensing/perception with communication and positioning/movement but is not collectively optimized. Individual losses can have uneven outcomes including the total loss of the system.
5. Class 4 Swarms. Each spacecraft exploits concurrent coordination of positioning/movement, communication, and sensing to perform system-level optimization. This system acts if it's a single entity. Communication, computation, and sensing are evenly distributed within the swarm. Individual losses result in a gradual loss in system performance.

Class 0 swarms have been successfully realized for several Earth applications (Grewal, Weill, and Andrews, 2007). We classify constellations such flower constellations (Mortari, Wilkins, and Bruccoleri, 2004) as Class 1 swarms due to the formations of their trajectories. Class 2 swarms are being developed for applications such as the deflection assessment of binary asteroids (Galvez, Carnelli, Michel, et al., 2013). Class 3 swarms have been used in interplanetary gravimetry applications (Zuber, D. E. Smith, Watkins, et al., 2013). A Class 4 swarm mission design is yet to be studied. Parametric mission design and mission cost modeling is well studied in the literature (Wertz, Everett, and Puschell, 2011). Existing research has also focused on the development of mission design tools for spacecraft swarms around Earth (Conn, A. Perez, Plice, et al., 2017). Due to the involvement of integer parameters, and nonlinear functions, many swarm design problems result in MINLP problems (Rao, 2019). Evolutionary algorithms, such as the genetic algorithm (Conn, A. Perez, Plice, et al., 2017), and

particle swarm optimizer (Kennedy and Eberhart, 1995), have provided robust solutions to MINLP optimization. Genetic algorithms have also been applied to spacecraft communication systems (Lohn, Linden, Hornby, et al., 2004), and trajectories (Hartmann, Coverstone, and Williams, 1998). Our previous work on IDEAS focused on developing the Automated Swarm Designer module of IDEAS, where we presented design optimization case studies of swarm missions to small bodies using genetic algorithm optimization. The developed case studies entail Class 0 swarms for Earth observation in Nallapu and Thangavelautham (2019b), and cis-lunar communications in Nallapu, Vance, Xu, et al. (2020); Class 1 swarms for global surface mapping of spinning asteroids were also designed in Nallapu and Thangavelautham (2019a); Class 2 swarms for RoI observation on spinning asteroids in Nallapu and Thangavelautham (2019c), global surface mapping of tumbling asteroids in Nallapu, Xu, Marquez, et al. (2020). Case studies to planetary moons include global surface through hyperbolic flybys Nallapu and Thangavelautham (2020), and polar resonant co-orbits in Nallapu and Thangavelautham (2019d). In the current work, we present the design optimization of Class 2 visual mapping swarm missions to planetary moons, for global surface mapping, and RoI observation, where swarm will be in arbitrarily oriented resonant co-orbits around the central planet.

3. Design Modelling

This section describes the models and parameters used in the current work. We begin by defining the coverage requirements of the two mission types in the current work. For the sake of computational simplicity, the motion of the spacecraft and the target moon is modeled assuming the spherical two body gravity from the central planet (Vallado, 2013). Furthermore, we assume that the COEs of the moon are known, and a rough shape model of the moon is available to estimate surface coverage.

3.1. Mission Design and Parameters

The coverage requirements associated with the two missions are as follows:

Global Surface Mapping. In these missions, the spacecraft are required to meet a minimum cumulative surface coverage $P_{Map,R}$ requirement, with a maximum ground resolution of x_R in one orbit of the moon.

RoI Observation. The RoI observation mission adds the temporal aspect of the coverage requirement, where the objective is to observe a target region of interest (RoI) on the moon's surface which is specified by its longitude $\varphi_{x,E}$ and latitude $\varphi_{y,E}$ and has a square angular spread of Φ_E as illustrated in Figure 2. The RoI is required to be imaged at a maximum resolution of x_R and needs to be observed for a minimum duration of $t_{RoI,R}$, with a minimum cumulative coverage requirement of $P_{RoI,R}$ in one orbit of the moon.

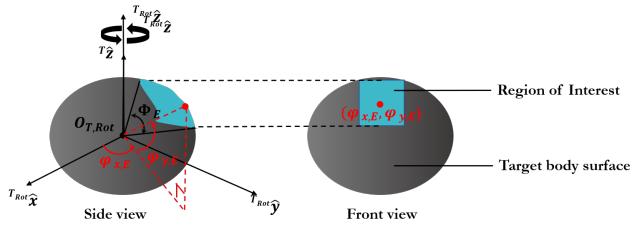

Figure 2: Parameters involved in defining the region of interest over the surface of the target body.

Spacecraft Camera Requirements. For a given spacecraft camera, the maximum flyby altitude h_{max} to meet the x_R requirement, and half-field of view of the camera η_C is computed as (Wertz, Everett, and Puschell, 2011)

$$h_{max} = \frac{x_R D_C}{\lambda_C} \tag{1}$$

and

$$\sin \eta_C = \left(\frac{r_{T,av}}{r_{max}} \right) \cos \epsilon_f \tag{2}$$

Where D_C and λ_C are the aperture diameter of the camera, and imaging wavelength of the camera sensor respectively. The parameter ϵ_f indicates a slant angle tolerance at the imaging radius r_{max} given by

$$r_{max} = r_{T,av} + h_{max} \tag{3}$$

Where $r_{T,av}$ is the average radius of the moon. Using an altitude tolerance Δh_f, the spacecraft will pass the target at a radial distance r_f given by

$$r_f = r_{max} - \Delta h_f \tag{4}$$

It should be noted here that r_f is not the minimum distance of the spacecraft to the moon, but is a point on the spacecraft trajectory where the visual coverage of the spacecraft meets the x_R requirement. The camera of the spacecraft is modeled as a pinhole camera with a square sensor (Sobel, 1972), whose pyramidal field of view (FoV) is used to model the instantaneous footprint of the camera on the surface of the target.

3.2. Swarm Configurations

The swarm will be configured to visit the moon over N_v encounters. During a visit j, the moon will be located at a true anomaly of $f_{v,j}$ on its orbit. Since

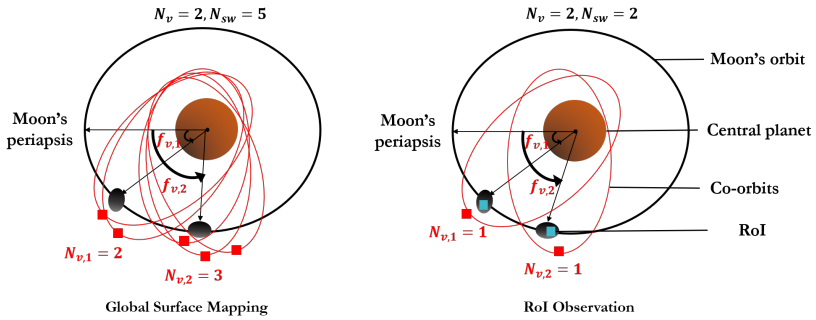

Figure 3: The configuration of the spacecraft swarms for in the global surface mapping (left) and ROI observation (right) missions.

the coverage requirements of the two missions are different, the co-orbits of the swarm will be configured differently for these two missions, as illustrated in Figure 3

Specifically, each encounter in the global surface mapping mission will contain multiple spacecraft, while in case of the RoI observation missions, each encounter will only contain a single spacecraft. Therefore, the number of spacecraft in case of the mapping mission can be expressed as

$$N_{Sw,map} = \sum_{j=1}^{N_v} N_{v,j} \tag{5}$$

where $N_{v,j}$ is the number of spacecraft in visit j. In the case of the RoI observation swarm, the number of spacecraft in the swarm can be expressed as

$$N_{Sw,RoI} = \sum_{j=1}^{N_v} 1 \;=\; N_v \tag{6}$$

3.3. Dynamical Models

Since the current problem involves simulating the motion of multiple entities such as the spacecraft, planets, and the target moon, the key reference frames used in the current work are described here:

Planetary Inertial Frame. The motion of the target moon and the spacecraft swarm is modeled in the inertial $J2000$ reference frame (Vallado, 2013) centered at the planet. The vectors in this planetary inertial frame will be denoted by N.

Target Moon Frames. Two key reference frames are used in the current to study the surface coverage of the moon.

Target Inertial A target centered inertial frame T is used to note the distance of the spacecraft to the moon. We construct the T frame by translating the N frame to the center of the target moon.

Target Fixed Since the moon is assumed to be a uniform rotator, we model the rotation of the surface in a target centered rotational frame T_{Rot}. The raw shape model of the target moon is described by a unique set of vertices V_T, and triangular face connectivity set F_T (Scheeres, 2016). For the sake of simplicity, we assume that the vertices of the raw shape model are described in the T_{Rot} frame with its z axis as the rotation pole as shown in Figure 2. Therefore, at a simulation time t, the vertices are expressed in the T frame using the principal z axis rotational transformation (Schaub and Junkins, 2013) of V_T by an angle $\theta_T(t)$. In order to enforce tidal locking (Aleshkina, 2009), we set $\theta_T(t)$ to

$$\theta_T(t) = \mod\left(f_0 + \left(\frac{2\pi}{P_T}\right)t, 2\pi\right) \tag{7}$$

Where f_0 is the true anomaly of the moon at the start of the simulation, and P_T is the orbital period of the moon.

3.4. Co-orbit Encounter

The co-orbits in the current work are designed such that the deployed spacecraft encounter the moon at the flyby distance noted from Equation 4 on their orbital apoapsis. Since only two body dynamics are considered, the COE description is used to define the spacecraft and moon orbits (Vallado, 2013). Here we derive constrain the COEs of the resonant co-orbits to model the spacecraft motion in the N frame.

True anomaly. Since the designed encounters occur on the apoapsis of the co-orbits, the true anomaly at the encounter epoch is given by $f_{Sw} = 180$ deg (Vallado, 2013).

Resonant Semi-major Axis. The resonance ensures that the spacecraft encounters with the moon will repeat after every p orbits of the moon or after every q orbits of the spacecraft. Using Kepler's third law (Vallado, 2013), we can write

$$\left(\frac{a_T}{a_{Sw}}\right)^{\frac{3}{2}} = \frac{p}{q} \tag{8}$$

where a_T and a_{Sw} are the semi-major axis of the moon and the spacecraft respectively. It can be noted from Equation 8 that p, q, and a_{Sw} do not depend on the location of the moon, and are therefore constant for all spacecraft in the swarm.

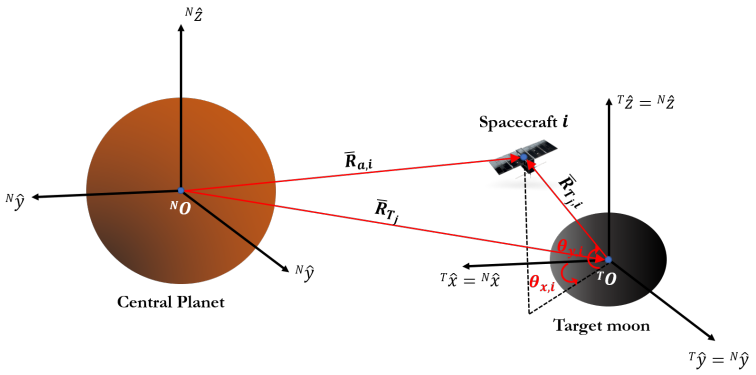

Figure 4: Geometrical parameters involved in defining the spacecraft apoapsis vectors.

Eccentricity. Since Equation 4 describes the spacecraft distance from the moon, two additional coordinates are required to describe the encounter in three dimensions. Let $\theta_{x,i}$, and $\theta_{y,i}$ denote the azimuth and elevation of spacecraft i during an encounter j as shown in in Figure 4. The corresponding apoapsis vector ${}^{N}\bar{R}_{a,i}$ is expressed as

$$ {}^{N}\bar{R}_{a,i} \;=\; {}^{N}\bar{R}_{T_j} \;+\; {}^{N}\bar{R}_{T_j i} \tag{9} $$

where ${}^{N}\bar{R}_{T_j}$ is the position vector of the moon to the central planet at a true anomaly $f_{v,j}$, and ${}^{N}\bar{R}_{T_j i}$ is given by

$$ {}^{N}\bar{R}_{T_j i} \;=\; r_f \left[\cos\theta_{x,i}\cos\theta_{y,i} \quad \sin\theta_{x,i}\cos\theta_{y,i} \quad \sin\theta_{y,i}\right]^T \tag{10} $$

The left superscript beside a vector indicates the reference frame in which the vector is resolved. It should be noted that while the left-hand side of Equation 10 is the spacecraft location with respect to the moon in the T frame, we set ${}^{T}\bar{R}_{T_j i} \;=\; {}^{N}\bar{R}_{T_j i}$ following the assumption that the T is constructed by a pure translation of the N frame. The eccentricity of the spacecraft co-orbit $e_{sw,i}$ and its periapsis altitude $h_{p,i}$ can then be determined as (Vallado, 2013)

$$ e_{sw,i} \;=\; \left(\frac{r_{a,i}}{a_{sw}}\right) \;-\; 1 \tag{11} $$

and

$$ h_{p,i} = a_{sw}\left(1 - e_{sw,i}\right) - R_{Pl} \tag{12} $$

Where $r_{a,i}$ is the magnitude of ${}^{N}\bar{R}_{a,i}$, and R_{Pl} is the radius of the central planet.

Boundary Values Using Equation 9, $r_{a,i}$ is bounded through the triangle inequality (Marghitu and Dupac, 2012) as

$$ \min\left(r_{T_j i}\right) - r_f \;\leq\; r_{a,i} \;\leq\; \max\left(r_{T_j i}\right) + r_f \tag{13} $$

Where $r_{T_j i}$ denotes the magnitude of ${}^{N}\bar{R}_{T_j i}$. The values of $\min(r_{T,j})$, and $\max(r_{T,j})$ occur at the moon's periapsis ($f_{v,j} = 0$ deg), and apoapsis ($f_{v,j} = 180$ deg) respectively (Vallado, 2013). Let $r_{a,B}$ denote the set of minimum and maximum boundary values of $r_{a,i}$, which allows us to compute the set of bounding eccentricities e_B using Equation 11. Additionally, the minimum periapsis altitude of the co-orbit $h_{p,min}$ is also computed using Equation 12. The boundary values are used to evaluate the feasibility of a specified resonance as described in the following subsections.

Orbital Orientation. The orientation orbital elements: the right ascension of the ascending node (RAAN), inclination, and argument of periapsis define a $z-x-z$ Euler angle rotation matrix to transform the orbit in a perifocal frame of the planet to the N frame (Schaub and Junkins, 2013). The task at hand, is to compute the orientation elements such that ${}^{N}\bar{R}_{a,i}$ of spacecraft i passes through the encounter location specified by $f_{v,j}$ (see Figure 3). However, for planar orbit insertions, the orientation orbital elements are constrained by the hyperbolic tube defined by the incoming excess velocity vector ${}^{N}\bar{V}^{-}_{\infty,2}$, and orbits whose orientation elements are not supported by the tube require an orientation change maneuver (Vallado, 2013). This couples the co-orbit design of the swarm with their interplanetary trajectory. Here we use the Triad algorithm (Schaub and Junkins, 2013) to determine the perifocal to N frame rotation matrix $[NP_i]$ of spacecraft i, and to estimate the maneuver cost associated with the orientation change $\Delta v_{OC,i}$.

Triad Construction We begin by assuming that ${}^{N}\bar{V}^{-}_{\infty,2}$, and the periapsis altitude of the arrival hyperbola $h_{p,0}$ are known ahead through trajectory design. The N frame vectors ${}^{N}\bar{R}_{a,i}$ and ${}^{N}\bar{V}^{-}_{\infty,2}$ can now be resolved in the perifocal frame P_i of spacecraft i (Vallado, 2013). A possible rotation matrix $[NP_i]$ can now be defined from the Triad algorithm as (Schaub and Junkins, 2013)

$$[NP_i] = [\hat{n}_1 \quad \hat{n}_2 \quad \hat{n}_3][\hat{p}_{i,1} \quad \hat{p}_{i,2} \quad \hat{p}_{i,3}]^T \tag{14}$$

where the unit basis vectors are defined as

$$\begin{aligned} \hat{n}_1 &= \frac{{}^{N}\bar{R}_{a,i}}{r_{a,i}} & \hat{p}_{i,1} &= \frac{{}^{P}_{i}\bar{R}_{a,i}}{r_{a,i}} \\ \hat{n}_2 &= \frac{{}^{N}\bar{R}_{a,i} \times {}^{N}\bar{V}^{-}_{\infty,2}}{\left|{}^{N}\bar{R}_{a,i} \times {}^{N}\bar{V}^{-}_{\infty,2}\right|} & \hat{p}_{i,2} &= \frac{{}^{P}_{i}\bar{R}_{a,i} \times {}^{P}_{i}\bar{V}^{-}_{\infty,2}}{\left|{}^{P}_{i}\bar{R}_{a,i} \times {}^{P}_{i}\bar{V}^{-}_{\infty,2}\right|} \\ \hat{n}_3 &= \hat{n}_1 \times \hat{n}_2 & \hat{p}_{i,3} &= \hat{p}_{i,1} \times \hat{p}_{i,2} \end{aligned} \tag{15}$$

The orientation elements of spacecraft i can be extracted from the rotation matrix $[NP_i]$ (Schaub and Junkins, 2013). While it appears that Equations 14, and 15 always provides a valid $[NP_i]$, the triad algorithm often looses information about the second reference vector, due to the cross product operation in defining $\hat{n}_2$ and $\hat{p}_{i,2}$. This allows us to write the error in $\Delta v_{OC,i}$ as

$$\Delta v_{OC,i} = [NP_i]^{P}_{i}\bar{V}^{-}_{\infty,2} - {}^{N}\bar{V}^{-}_{\infty,2} \tag{16}$$

We interpret $\Delta v_{OC,i}$ as the maneuver cost of spacecraft i to correct ${}^{N}\bar{V}^{-}_{\infty,2}$ and have the same orientation elements of the selected co-orbit. The 6 COEs presented here describe the design of the resonant co-orbit which facilitates an apoapsis encounter with the moon.

3.5. Trajectory Design with Aerobraking

Using Lambert's solver, the excess velocity vectors can be determined for a given launch epoch D_L, and arrival epoch D_A, from which we determine the characteristic energy at Earth launch $C_{3,E}$, time of flight TF and ${}^{N}\bar{V}^{-}_{\infty,2}$ (Vallado, 2013). It should be noted here that while the focus of the current work is the design of swarm missions, we only note a single pair of launch and arrival epochs. We assume that the swarm is launched from a single launch provider (Schoolcraft, Klesh, and Werne, 2016). However, the launch configurations are not addressed in the current work. Assuming that the central planet has sufficient atmosphere, the spacecraft in the swarm will be designed to enter into their desired co-orbits though the aerobraking maneuver. This aeroassist occurs in four phases: HEO capture, walk-in, main phase, walk-out (Vallado, 2013). In the current work, we use simplified models for these four phases where the aerobraking occurs at a fixed periapsis altitude h_A from the surface of the planet using impulsive tangential maneuvers. During the HEO capture, the spacecraft perform an insertion maneuver at their periapsis located at an altitude $h_{p,0}$ from the surface of the central planet, into a high eccentricity orbit (HEO) with an eccentricity e_1. Let $r_{a,HEO}$ denote the apoapsis radius of this orbit. During the Walk-in phase, the spacecraft perform a maneuver at their HEO apoapsis to reduce their periapsis altitude to h_A. Let e_{I_1} denote the eccentricity of this intermediate orbit. This begins the main phase where, upon periapsis passage, the altitude of apoapsis reduces while the periapsis altitude remains the same, without the need for additional maneuvers. However, it is acknowledged here that in reality additional maneuvers are required to maintain the periapsis altitude during the main phase (Spencer and Tolson, 2007). Once the apoapsis radius falls to the target value described by $r_{a,i}$, they perform a maneuver at their apoapsis, to increase the periapsis altitude from h_A to their corresponding $h_{p,i}$. Since the $r_{a,i}$ and $h_{p,i}$ vary for each spacecraft in the swarm, we use their boundary values to estimate the maximum velocity change $\Delta v_{OI,max}$ required for orbit insertion with aerobraking. Let $e_{I_2,B}$ denote the boundary value (either maximum or minimum) of the eccentricity of the intermediate spacecraft orbit after the main aerobraking phase corresponding to an apoapsis radius of $r_{a,B}$. Then the $\Delta v_{OI,max}$ can be expressed as (Vallado, 2013)

$$\Delta v_{OI,max} \;=\; \Delta v_{HEO} \;+\; \Delta v_{WI} \;+ \max\left(\Delta v_{WO,B}\right) \tag{17}$$

Where

$$
\begin{aligned}
\Delta v_{HEO} &= \sqrt{v_{\infty,2}^2 + \frac{2\mu_{Pl}}{h_{p,0} + R_{Pl}}} - \sqrt{\frac{\mu_{Pl}\,(1+e_1)}{h_{p,0} + R_{Pl}}} \\
\Delta v_{WI} &= \sqrt{\frac{\mu_{Pl}\,(1-e_1)}{r_{a,HEO}}} - \sqrt{\frac{\mu_{Pl}\,(1-e_{I_1})}{r_{a,HEO}}} \\
\Delta v_{WO,B} &= \sqrt{\frac{\mu_{Pl}\,(1-e_{I_2,B})}{r_{a,B}}} - \sqrt{\frac{\mu_{Pl}\,(1-e_B)}{r_{a,B}}}
\end{aligned}
\tag{18}
$$

where μ_{Pl} denotes the gravitational parameter of the central planet, and $v_{infty,2}$. The intermediate elements e_{I_1}, $r_{a,HEO}$, and $e_{I_2,B}$ can be computed from the conic section geometry (Vallado, 2013). The boundary values of $r_{a,B}$ and e_B can be noted through Equations 13 and 11. We interpret $\Delta V_{OI,max}$ as the worst case maneuver cost required for capture assuming only planar maneuvers.

3.6. Swarm Behavior

All spacecraft are assumed to be identical in terms of subsystems, and the identical design is referred to as the seed spacecraft. However, their behavior will follow the Class 2 behavior described in Nallapu and Thangavelautham (2019c), where the swarm has a Leader spacecraft, while the remaining are the Observer spacecraft. The Leader, in addition to mapping, will gather the information from the Observers and relay it to a ground station on Earth when its distance to the moon exceeds r_{max}. A distance-based selection algorithm described in Nallapu and Thangavelautham (2019d) is used to identify the leader spacecraft in the swarm. The swarm architecture is summarized in Figure 5. In the current work, the communication interaction between the spacecraft is not described, and only the mapping behavior is studied.

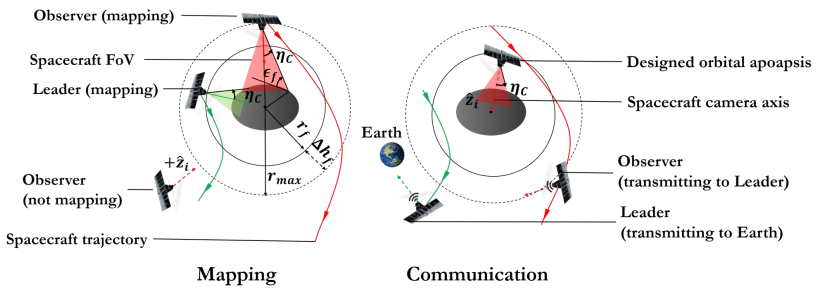

Figure 5: Behavior of different spacecraft in the Class 2 swarm described in the current work.

Spacecraft. The spacecraft is modeled as a rigid body, with the camera mounted along the z axis of its body frame as shown in 5. During a mapping operation, we assume that all spacecraft track the reference attitude described in Tsiotras,

Shen, and Hall, 2001, where the camera tracks the line of sight (LoS) to a specified point. For the global surface mapping missions, this specified point is the center of the target moon (shown in Figure 5), while in the RoI observation mission, this is the point on the surface located at spherical co-ordinates $r_{T,av}$, $\varphi_{x,E}$, and $\varphi_{y,E}$.

3.7. Coverage Evaluation

To provide a generalized description of the coverage algorithms for both missions, we consider the coverage of sub-region described by faces $F_{TR} \subseteq F_T$. Furthermore, we assume that the vertices in V_T are expressed in the T frame. We use a series of 3 filters on V_T and F_{TR} to estimate the instantaneous and cumulative coverage of the moon: illumination, LoS culling, and clipping (Nallapu and Thangavelautham, 2019d). The three filters are described as follows:

Illumination. At a time t, the set of faces that are illuminated by the Sun are noted using the inner product between the moon-to-Sun direction ${}^{T}\hat{R}_{TH}$ and the normal vector to each face. If ${}^{T}\hat{n}_{k,TR}$ denotes the instantaneous normal vector of face k in F_{TR}, the face is considered illuminated if ${}^{N}\hat{R}_{TH}.{}^{T}\hat{n}_{k,TR} > 0$. This filters out the set of all illuminated faces $F_l(t) \subset F_{TR}$ at t. However, an exception to this rule is when the Sun direction is eclipsed by the transiting planet, as described in Nallapu and Thangavelautham (2019d). When this happens all faces are considered to be shadowed, and will not be observed.

LoS Culling. The faces in $F_l(t)$ are culled with respect to the line of sight (LoS) from spacecraft to the specified point on the target. Let ${}^{T}\bar{R}_{Ti}$ denote the position vector of spacecraft i with respect to target, and ${}^{T}\hat{n}_{k,l}$ denote the normal vector of face k in $F_l(t)$ at t. The face with ${}^{T}\bar{R}_{Ti}.{}^{T}\hat{n}_{k,l} \leq 0$ will not be observed by the spacecraft. This operation further filters the set of illuminated faces that face the spacecraft i $F_{C,i}(t) \subseteq F_l(t)$.

Clipping. While the above two operations filter the faces, the clipping operation filters the vertices of $F_{C,i}$ which fall inside the FoV of spacecraft i. In the clipping operation, we construct the camera transformation matrix, which transforms the FoV into a unit cube (Sobel, 1972). The instantaneous camera transformation matrix G_i into the image space of spacecraft i is given by

$$G_i \ = VT_1T_2 \tag{19}$$

.

where

$$T_1 \ = \ \begin{bmatrix} [TB_i] & 0 \\ 0 & 1 \end{bmatrix}_{4\times 4} \tag{20}$$

$$T_2 \;=\; \begin{bmatrix} [I_{3\times 3}] & -\bar{R}_{Ti} \\ 0 & 1 \end{bmatrix}_{4\times 4} \tag{21}$$

.

and

$$V \;=\; \begin{bmatrix} \cot\eta_C & 0 & 0 & 0 \\ 0 & \cot\eta_C & 0 & 0 \\ 0 & 0 & \frac{fa_C \,+\, ne_C}{fa_C \,-\, ne_C} & \frac{-2fa_C\ ne_C}{fa_C \,-\, ne_C} \\ 0 & 0 & 1 & 0 \end{bmatrix}_{4\times 4} \tag{22}$$

The matrix $[TB_i]$ is the rotation matrix that transforms the body frame of spacecraft i to the T frame, and $[I_{3\times 3}]$ is the 3×3 identity matrix. The LoS tracking reference attitude described in Tsiotras, Shen, and Hall, 2001 is used to model $[TB_i]$. The parameters ne_C, and fa_C indicate the near field and far field distance of the spacecraft's camera. Here, we set $fa_C \;=\; h_{max}$, and select an arbitrary small value of ne_C for the spacecraft camera. Let $[{}^{N}a \quad {}^{N}b \quad {}^{N}c]^T$ denote the position vector of a vertex that forms at least one triangular face in $F_{C,i}(t)$. The vertex is resolved in an intermediate camera space Ci of spacecraft i by using the camera transformation

$$\left[{}^{Ci}a \quad {}^{Ci}b \quad {}^{Ci}c \quad {}^{Ci}d\right]^T \;=\; G\left[{}^{N}a \quad {}^{N}b \quad {}^{N}c \quad 1\right]^T \tag{23}$$

.

Where ${}^{Ci}d$ is the apparent depth of the projection. The camera space is normalized by ${}^{Ii}d$ to obtained the scaled coordinate in the image frame Ii of spacecraft i, ie,

$$\left[{}^{Ii}a \quad {}^{Ii}b \quad {}^{Ii}c\right]^T \;=\; \frac{1}{{}^{Ci}d}\left[{}^{Ci}a \quad {}^{Ci}b \quad {}^{Ci}c\right]^T \tag{24}$$

.

The vertex $[{}^{N}a \quad {}^{N}b \quad {}^{N}c]^T$ will fall inside the FoV of spacecraft i if the absolute value of its coordinates lies in a unit cube (Sobel, 1972).

$$\text{abs}\left(\left[{}^{Ii}a \quad {}^{Ii}b \quad {}^{Ii}c\right]^T\right) \;<\; \left[1 \quad 1 \quad 1\right]^T \tag{25}$$

.

If a vertex fails the clipping criterion in Equation 25, all faces in $F_{C,i}(t)$ that are formed by it are omitted from the coverage computation. The final result of these three filters is a set of faces $F_{FoV,i}(t)$ whose faces are illuminated by the Sun, and whose vertices fall inside the FoV of spacecraft i at a time t.

Instantaneous Coverage. At time t, the set of faces observed $F_{Ins}(t)$ is computed as

$$F_{Ins}(t) = \bigcup_{i=1}^{N_{Sw}} F_{FoV,i}(t) \tag{26}$$

Where N_{Sw} is the number of total spacecraft in the swarm. To reduce the computational load, only those spacecraft whose distance to the target is below r_{max} are used in the computation of Equation 26. The three filters described here are illustrated in Figure 6.

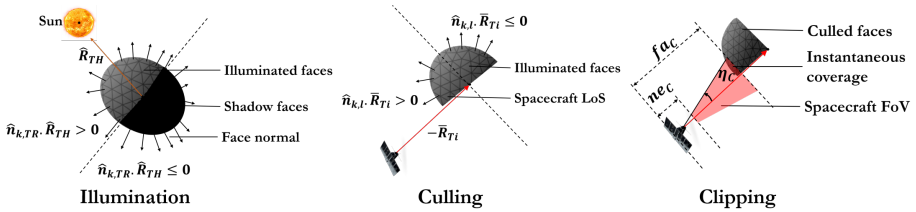

Figure 6: Illustration of the three filters used to model the instantaneous spacecraft coverage.

Cumulative Coverage. Similarly, we note the cumulative faces $F_{Cum}(t_{sim})$ observed up to the simulation time t_{sim} as

$$F_{Cum}(t_{sim}) = \bigcup_{t=0}^{t_{sim}} F_{Ins}(t) \tag{27}$$

Figures of Merit. The area of surface described by faces in $F_{Cum}(t_{sim})$ is the sum of areas of their triangular areas (Goldman, 1991). Let $A_{Cum}(t_{sim})$ and A_{TR} denote the cumulative surface area of the faces $F_{Cum}(t_{sim})$ and F_{TR} respectively. Then the figure of merit considered in the current work is the cumulative percentage of surface coverage given by,

$$P_{Cum}(t_{sim}) = \frac{A_{Cum}(t_{sim})}{A_{TR}} \times 100 \tag{28}$$

This allows us to define the individual figures of merit specific to the two different missions described in the current work as follows:

Global Surface Mapping For global surface mapping, we set $F_{TR} = F_T$ for evaluating the coverage over the entire surface. The corresponding cumulative percentage of surface coverage by the swarm, computed from Equation 28, is denoted by $P_{map}(t_{sim})$.

RoI Observation For RoI observation, we set $F_{TR} = F_{RoI}$, which is the set of surface faces that lie inside the RoI. The faces in F_{RoI} are modeled by using the clipping operation, where a virtual camera is placed at the center of the target body, and the viewing direction is located along the position vector from the moon center to the RoI location. In the case of the RoI mission, the corresponding cumulative percentage of surface coverage by the swarm is denoted by $P_{RoI}(t_{sim})$. Additionally, since the RoI observation is a time-based mission, we also measure the simulation time t_{RoI} for which the RoI was in the FoV of at least one spacecraft.

3.8. Collision Avoidance

We design the spacecraft trajectories to be ballistically free of collisions using a binary collision flag parameter. Specifically, we check if the trajectories: i. collide with the moon and ii. collide with other spacecraft in the swarm. Collisions with the central planet are avoided by placing a minimum periapsis altitude constraint on the trajectory design. The moon and spacecraft collisions are checked as follows:

Moon Collisions. By propagating the orbital motion of the spacecraft, we note the magnitude of the distance of spacecraft i to the moon r_{Ti} throughout the simulation time. we require that $r_{Ti} > r_{T,max}$, for all $i = 1, 2, ...N_{Sw}$, in the time span $[0,\ T_{sim}]$. Here $r_{T,max}$ is the maximum radius of the target shape model.

Spacecraft Collisions. Using a similar approach, if $r_{i,l}$ denotes the magnitude of position vector from spacecraft i to spacecraft l, we require that $r_{il} > r_{col}$, for all $i, j = 1, 2, ...N_{Sw}$ and $i \neq l$, in the complete simulated time span $[0,\ T_{sim}]$. Here, r_{col} indicates a collision radius around each spacecraft.

The collision flag is set to 0 if all spacecraft co-orbits are free of the moon, and spacecraft collisions, and is 1 otherwise.

3.9. Spacecraft Design

While in the planned architecture of IDEAS (in Figure 1), the spacecraft designer module is programmed into the software, in the current work, we use a seed spacecraft template with commercially available off-the-shelf small spacecraft subsystems. The composition of the seed spacecraft dry mass used is presented in Appendix A.

Wet mass. To ensure that the spacecraft in the swarm is capable of the two maneuvers: orbit insertion, and orientation change, the seed spacecraft is allotted fuel enough to perform a total velocity change Δv_{net} given by

$$\Delta v_{net} = 1.3\left(\Delta v_{OI,max} + \max\left(\Delta v_{OC,i}\right)\right) \tag{29}$$

The factor 1.3 is used as a 30 % margin to account for correction maneuvers due to unmodeled dynamics (Vallado, 2013; Scheeres, 2016). The fuel mass of

the seed spacecraft and its wet mass at launch is noted from the rocket equation (Vallado, 2013).

Cost Estimation.

Seed Spacecraft Mission Using the wet mass of the seed spacecraft, we estimate the seed spacecraft mission cost using empirical cost models. Specifically, we use the small satellite cost model (SSCM) to estimate the bus and mission operation cost (Mahr, Tu, and Gupta, 2016), and the NASA instrument cost model (NICM) to estimate the cost of the camera (Habib-Agahi, Ball, and Fox, 2009). The models used in the current work, estimate the cost in United States Dollar currency, in the fiscal year 2010 (FY$10), and is converted to millions of launch year dollars (LY$M) using its launch year inflation factor (Wertz, Everett, and Puschell, 2011). Using the SSCM and NICM models we estimate the total mission cost TM_1, and standard error SE_{M1} associated with one seed spacecraft.

Launch. The launch cost is estimated using a database of launch providers presented in Wertz, Everett, and Puschell, 2011. Using the database, we note the lowest launch cost LC_1 and the corresponding standard error SE_{L1} of a single seed spacecraft. It should be noted that the SSCM, and the launch cost models used in the current work estimate costs of Earth-based missions. However, we use the multiplicative interplanetary factor from the QuickCost model (Wertz, Everett, and Puschell, 2011) to estimate the cost for the interplanetary mission.

Swarm Mission. Since all the spacecraft are assumed to have the same seed spacecraft design, the total space segment cost of the swarm mission and its standard error are expressed as (Wertz, Everett, and Puschell, 2011)

$$TC_S \ = TM_1 \times N_{Sw}^{\left(1 \ + \ \frac{\ln S}{\ln 2}\right)} \ + \ (N_{Sw} \times LC_1) \tag{30}$$

$$SE_S \ = \sqrt{N_{Sw}} \sqrt{{SE_{M1}}^2 \ + \ {SE_{L1}}^2} \tag{31}$$

Where S is a learning curve factor from designing identical spacecraft. It is acknowledged here that the accuracy of the cost models is quite limited given that the models can be outdated by the rapid advancement in spacecraft technology (Weston, Miller, Ingersoll, et al., 2018). However, the costs noted here can still be useful in the early mission design phase as a crude baseline estimate.

4. Design Optimization

In this section, we formulate the MINLP problems corresponding to the optimal trajectory and swarm design modules in case of the two swarm missions. For simplicity, we use the same trajectory design problem for both missions.

Trajectory Design. We use the Automated Trajectory Designer module to minimize the objective function $J_{Tr} = \Delta v_{OI,max}$. We place upper bound constraints on $C_{3,E}$, TF, $v_{\infty,2}$, and a lower bound constraint on $h_{p,min}$ which ensures that the spacecraft will not collide with the central planet. Additionally, we eliminate impractical solutions through linear constraints that enforce the launch epoch D_L occurs before the arrival epoch D_A, and the number of spacecraft orbits q is greater than the number of moon's orbits p. This is to ensure that the orbits of the spacecraft have a smaller semi-major axis than that of the target moon. The trajectory design optimization problem for both missions is therefore presented as 32.

$$\begin{aligned} \min \quad & J_{Tr} = \Delta v_{OI,max} \\ \text{s.t.} \quad & C_{3,E} - C_{3,max,R} \leq 0 \\ & TF - TF_{max,R} \leq 0 \\ & v_{\infty,2} - v_{\infty,2,max,R} \leq 0 \\ & h_{p,min,R} - (h_{p,min}) \leq 0 \\ & D_L - D_A \leq 0 \\ & p - q \leq 0 \end{aligned} \tag{32}$$

The trajectory design decision vector is shown in Figure 7. All design variables of the decision vector are bounded by user input values. The epochs D_L, and D_A are formatted in the Julian time format and are used to note the positions of the Earth and the target planet using an analytical planetary ephemeris model (Vallado, 2013). The Lambert problem on the D_L and D_A epochs is solved using the Gooding's algorithm (Gooding, 1990).

Parameter	Launch epoch	Arrival epoch	Hyperbolic Periapsis altitude	HEO Eccentricity	Resonance Parameters	
					# Target Orbits	# spacecraft Orbits
Variable	D_L	D_A	$h_{p,0}$	e_0	p	q
Range	Real $[D_{L,min}, D_{L,max}]$	Real $[D_{A,min}, D_{A,max}]$	Real $[h_{p,min,R}, \infty)$	Real $[0, e_{1,max}]$	Integer $[p_{min}, p_{max}]$	Integer $[q_{min}, q_{max}]$

Figure 7: Design variables of the trajectory design problem, and their corresponding ranges.

4.1. Swarm Design

We use the Automated Swarm Designer module to design swarms that can meet the coverage, collision, and trajectory performance requirements with a minimum number of spacecraft. The design problems specific to each problem is expressed as follows:

Global Surface Mapping. In the global surface mapping application, we minimize the objective function $J_{Sw,map} = N_{Sw,map}$ such that the cumulative coverage of the swarm exceeds the coverage requirement $P_{map,R}$ without any

collisions, with the maximum value of $\Delta v_{OC,i}$ upper bounded by $\Delta v_{OC,max}$. The problem can be expressed as

$$\begin{aligned} \min \quad & J_{Sw,map} = N_{Sw,map} \\ \text{s.t.} \quad & P_{map,R} - P_{map}(t_{sim}) \leq 0 \\ & \text{Collision flag} \leq 0 \\ & \max(\Delta v_{OC,i}) - \Delta v_{OC,max} \leq 0 \end{aligned} \tag{33}$$

The decision vector of the global surface mapping problem is presented in Figure 8.

Parameter	# moon encounters	# Spacecraft each encounter			True anomaly of the moon			Spacecraft azimuth at encounter			Spacecraft elevation at encounter		
Variable	N_v	$N_{v,1}$	…	N_{v,N_v}	$f_{v,1}$	…	f_{v,N_v}	$\theta_{x,1}$	…	$\theta_{x,N_{Sw}}$	$\theta_{y,1}$	…	$\theta_{y,N_{Sw}}$
Range	Integer $[1, N_{1,max}]$	Integer $[1, N_{2,max}]$			Real $[0, 360]$ deg			Real $[0, 360]$ deg			Real $[-90, 90]$ deg		

Figure 8: Design variables of the global surface mapping swarm problem, and their corresponding ranges.

RoI Observation. In the RoI observation mission, we minimize $J_{Sw,RoI} = N_{Sw,RoI}$ such that the cumulative RoI coverage exceeds the spatial requirement $P_{RoI,R}$, and temporal requirement $t_{RoI,R}$, without collisions. The maximum value of $\Delta v_{OC,i}$ also assumed to be upper bounded by $\Delta v_{OC,max}$. The problem is expressed as

$$\begin{aligned} \min \quad & J_{Sw,RoI} = N_{Sw,RoI} \\ \text{s.t.} \quad & P_{RoI,R} - P_{RoI}(t_{sim}) \leq 0 \\ & t_{RoI,R} - t_{RoI} \leq 0 \\ & \text{Collision flag} \leq 0 \\ & \max(\Delta v_{OC,i}) - \Delta v_{OC,max} \leq 0 \end{aligned} \tag{34}$$

The decision vector of the global surface mapping swarm design problem is presented in Figure 9.

Parameter	# moon encounters	True anomaly of the moon			Spacecraft azimuth at encounter			Spacecraft elevation at encounter		
Variable	N_v	$f_{v,1}$	…	f_{v,N_v}	$\theta_{x,1}$	…	$\theta_{x,N_{Sw}}$	$\theta_{y,1}$	…	$\theta_{y,N_{Sw}}$
Range	Integer $[1, N_{1,max}]$	Real $[0, 360]$ deg			Real $[0, 360]$ deg			Real $[-90, 90]$ deg		

Figure 9: Design variables of the RoI observation swarm problem, and their corresponding ranges.

The bounds on all design variables shown in Figures 8 and 9 are provided through the user interface (illustrated in Figure 11). Since Equations 32, 33,

and 34 contain nonlinear constraints, and both real and integer variables, we classify them as MINLP problems. It should be noted that the swarm decision vector allow us to compute the spacecraft locations at the encounter instant, as described in Section 3.4. However at the start of simulations, we initialize the location of the moon by offsetting the lowest encounter true anomaly by Δf_0, ie,

$$f_0 \;=\; \min\left(f_{v,j}\right) \;-\; \Delta f_0 \tag{35}$$

The true anomalies of all spacecraft are then phased such that when the moon reaches a true anomaly of $f_{v,j}$, the spacecraft corresponding to this encounter reach a true anomaly of 180 deg (Vallado, 2013). The cumulative coverage is noted by propagating spacecraft, and moon motion for one orbital period of the moon.

4.2. Optimization Procedure

The inbuilt genetic algorithm (GA) solver of MATLAB explicitly allows optimization of MINLP problems (Deep, Singh, Kansal, et al., 2009), which made GA as the primary optimization solver. However, we also use the particle swarm optimization (PSO) solver (Kennedy and Eberhart, 1995) to compare the feasibility of the solutions and the performance of the optimizers. Both GA and PSO solvers are population-based optimizers, which iteratively explores a population of decision vectors (Rao, 2019). We use a stall stop criterion to identify a candidate optimal solution, where if the minimum value of the objective function is held constant for a defined number of iterations, a decision vector corresponding to this stalling minimum value is selected as the final solution. However, to avoid selecting a local optimal solution, we run multiple trials of optimization using each optimizer. The swarm design problems are computationally expensive: at a given simulation time, the instantaneous coverage scales as $\mathcal{O}\left(N(F_T) \times N_m\right)$, where $N(F_T)$ is the number of faces in the shape model, and N_m is the number of spacecraft participating in the mapping operations. As a means to overcome the computational bottlenecks, parallel computation architecture was a critical decision factor in selecting the two optimization solvers. A comparison of the two optimization algorithms considered in the current work is presented in Table 1. As seen here, the inbuilt PSO solver in MATLAB is not programmed to handle constraints and integer variables. Therefore the optimization problems in Equations 32, 33, and 34 were modified as real unconstrained optimization problems described as follows.

Unconstrained Optimization. We use the penalty function method (Rao, 2019) to convert the three optimization problems in Equations 32, 33, and 34 into unconstrained optimization. We note that the optimization functions in Equations 32, 33, and 34 can be generalized as

$$\begin{aligned} \min \quad & J \\ \text{s.t.} \quad & g_m(x) \;\leq\; 0 \quad m \;=\; 1, 2, ...N_C \end{aligned} \tag{36}$$

Table 1: Trade study showing a comparison of key features between the two optimization algorithms considered in the current work, and the primary optimizer algorithm (GA).

Feature	Solver	
	Genetic Algorithm	Particle Swarm Optimizer
Supports parallel computation architecture ?	Yes	Yes
Explicit accommodation of boundary constraints ?	Yes	Yes
Explicit accommodation of linear constraints ?	Yes	No
Explicit accommodation of nonlinear constraints ?	Yes	No
Explicit accommodation of integer variables ?	Yes	No

Where J is the objective function, g_m is the constraint m on the design, and N_c is the total number of constraints, which are functions of the generalized decision vector x. Then using the penalty method (Rao, 2019), the unconstrained problem with will optimize the modified objective function J^* given by

$$J^* = \begin{cases} J & \text{if } g_m(x) \leq 0 \; \forall \; m \\ J_{max} + \sum_{m=1}^{N_c} \langle g_m(x) \rangle & \text{otherwise} \end{cases} \tag{37}$$

Where J_{max} is the maximum value of the objective function. The operation $\langle y \rangle$ outputs the argument y if $y > 0$, or 0 otherwise. The penalty function in by Equation 37 is similar to the implicit penalty function of the GA solver in MATLAB (Deb, 2000). However, the key difference is the definition of the value of J_{max}: the GA solver implicitly computes a population-based J_{max} at each iteration, while we use a fixed value of J_{max} when solving the optimization problem with the PSO solver.

Real-Valued Programming. When using the PSO solver, all integer decision variables: p, q, N_v, and $N_{v,j}$ are rounded to their largest neighbouring integer.

5. Numerical Simulations

We now present numerical case studies to design the two visual mapping missions to explore the Martian moon Deimos. We begin by describing the model-specific parameters involved in defining the two swarm missions. The performance of the optimizers, trajectory, swarm, and spacecraft designs are then examined.

5.1. Mission and Simulation Parameters

Mission Definition. The coverage requirements and parameters in the definition of both missions are presented as follows::

Global Surface Mapping To map at least $P_{map,R} = 90$ % surface of Deimos with a maximum resolution of $x_R = 1$ m using a minimum sized Class 2 swarm deployed on resonant co-orbits around Mars. The coverage requirements of the global surface mapping mission are presented in Table 2.

Table 2: Mission definition parameters for the global surface mapping mission.

Parameter	Value
Surface coverage requirement, $P_{map,R}$	90 %
Desired resolution, x_R	1 m

RoI Observation To observe at least $P_{RoI,R} = 90$ % of a target RoI on the surface of Deimos located at $(\varphi_{x,E},\ \varphi_{y,E}) = (45,\ 45)$ deg with an angular spread of $\Phi_E = 15$ deg for at least $t_{RoI,R} = 20$ mins and a maximum resolution of at least $x_R = 1$ m. The swarm designed here will use a minimum sized Class 2 swarm that is deployed on resonant co-orbits. The coverage requirements of the RoI observation swarm mission are presented in Table 3.

Table 3: Mission definition parameters for the RoI observation mission.

Parameter	Value
RoI location, $(\varphi_{x,E}, \varphi_{y,E})$	$(45, 45)$ deg
RoI angular spread, Φ_E	15 deg
RoI observation time requirement, $t_{RoI,R}$	20 mins
RoI coverage requirement, $P_{RoI,R}$	90 %
Desired resolution, x_R	1 m

The orbital ephemeris and constants to model the motion of Deimos (Murray and Dermott, 1999; Giorgini, 2015), and the spacecraft are presented in Table 4. The aerobraking altitude was selected based on the walk-in phase aerobraking altitude of the Mars Odyssey mission (Smith Jr and Bell, 2005).

Table 4: Parameters used in the current work to model the motion of Deimos.

Parameter	Value
Deimos semi-major axis	23484 km
Deimos eccentricity	0.0002
Deimos inclination	1.78 deg
Deimos RAAN	261.5 deg
Deimos argument of periapsis	123 deg
Deimos orbital period	1.26 days
Mars gravitational parameter	43824 km^3/s^2
Mars equatorial radius	3394 km
Aerobraking altitude at Mars	150 km

Shape Model A 5400 triangular face shape model of Deimos (Thomas, Yoder, Synnott, et al., 2000) is used for coverage estimation. The average, and maximum radii noted from the shape model were 5.81 km, and 8.76 km respectively. The computed surface area was 519 km^2. The designed RoI spanned a total of 58 triangular faces, amounting to a total surface area of 5.94 km^2. The triangulated shape model of Deimos and surface faces corresponding to the RoI are presented in Figure 10. The heliocentric orbit of Mars is propagated using an analytical Julian time-based model of Martian ephemeris (Vallado, 2013). The motion of Deimos, and spacecraft are propagated for a simulation time $t_{sim} = 1.4$ days in order to allow a complete orbit of Deimos. The fixed simulation parameters for all simulations are presented in Table 5.

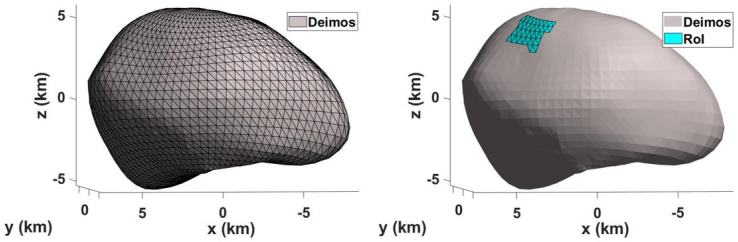

Figure 10: The shape model of Deimos showing the complete set of triangulated faces (left), and the RoI faces (right)

Table 5: Common simulation parameters used for designing the two missions considered in the current work.

Parameter	Value
Camera elevation angle, ϵ_f	20 deg
Flyby altitude tolerance, Δh_f	5 km
Initial true anomaly offset, Δf_0	1 deg
Collision radius, r_{col}	1 m
Learning factor for swarm cost, S	0.95
Simulation time span	[0, 1.3] days
Simulation time step	5 sec

The simulation architecture of the current work is presented in Figure 11. A Comparison of Figure 11 with Figure 1 also indicates the current development phase of the IDEAS software.

Flyby and Camera. The seed spacecraft in the current work is noted from Appendix A, and its required parameters are presented in Table 6. The red spectrum is used as the baseline imaging wavelength (Wertz, Everett, and Puschell, 2011). Using Equation 1, we note that the camera should be placed at $h_{max} = 114$ km which is used for fa_C to evaluate coverage. The half-Fov of the camera is noted as $\eta_C = 2.84$ deg from Equation 2.

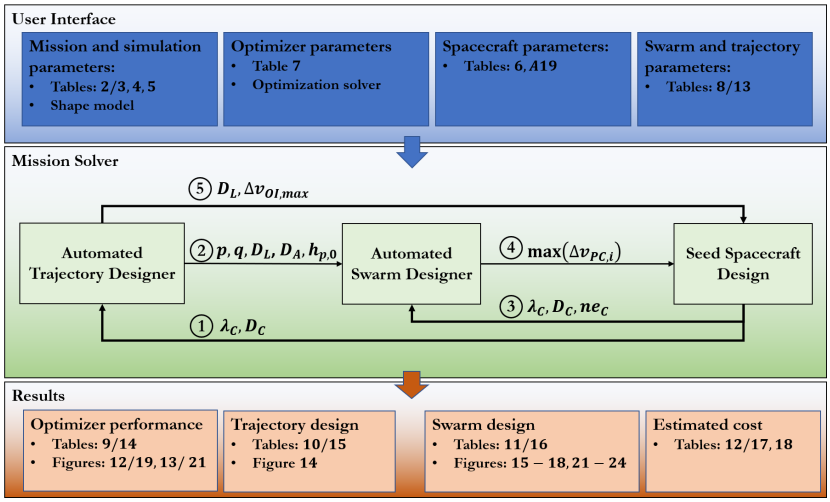

Figure 11: Architecture of the simulations in the current work, showing the sequential flow of information across the different design modules.

Table 6: Spacecraft camera and flyby parameters used in the current work.

Parameter	Value
Aperture diameter D_C	8 cm
Imaging wavelength λ_C	700 nm
Camera near-field distance ne_C	1 cm

Optimizer Setup. To facilitate a fair comparison between the optimizer performances, we use the same iteration search parameters for both GA and PSO solvers as shown in Table 7. All simulations were run on a high-performance computer cluster with a 2.3 GHz Intel Xeon Processor and were executed in a parallelized architecture with 14 processor cores. Each design problem was solved 5 times to verify if the final selected solution was a local optimal solution. A stall limit of 100 iterations was used to select the final solution in each trial. The solutions of the individual mission designs are described as follows:

5.2. Global Surface Mapping

The input parameters required for trajectory and swarm defination parameters used in the global surface mapping mission simulations are presented in Table 8. The results of the trajectory and swarm optimization are described as follows:

Trajectory Optimization. The variation of the least value of J_{Tr} noted from all optimization trials of Equation 32 is presented in Figure 12. As seen here, the PSO solver converged to its final solution in relatively fewer solutions. The lowest value of $\Delta v_{OI,max}$, was noted as 0.664 km/s among all GA design simulations, while it was 0.659 km/s among all PSO simulations.

Table 7: Parameters used in the current work to configure the optimization solvers

Design Problem	Parameter	Value
Trajectory	Population size per iteration	1000
	Maximum # iterations	1000
	Maximum # stall iterations	100
Global surface mapping	Population size per iteration	100
	Maximum # iterations	300
	Maximum # stall iterations	100
RoI Observation	Population size per iteration	500
	Maximum # iterations	300
	Maximum # stall iterations	100

Table 8: Trajectory and swarm definition parameters used in global surface mapping mission design.

Design Problem	Parameter	Value
Trajectory	Maximum launch energy, $C_{3,max,R}$	$20\ \mathrm{km^2/s^2}$
	Maximum time of flight, $TF_{max,R}$	200 days
	Maximum excess velocity at arrival, $v_{\infty,2,max,R}$	3 km/s
	Minimum Periapsis altitude, $h_{p,min,R}$	300 km
	Launch epoch bounds, $[D_{L,min}, D_{L,max}]$	[1/1/20, 00: 00 hr, 12/31/20, 00: 00 hr]
	Arrival epoch bounds, $[D_{A,min}, D_{A,max}]$	[5/1/20, 00: 00 hr, 12/31/21, 00: 00 hr]
	Maximum HEO eccentricity, $e_{1,max}$	0.98
	Resonance bounds, $[p_{min}, p_{max}]$	[1, 10]
	Resonance bounds, $[q_{min}, q_{max}]$	[1, 20]
	Maximum objective for PSO solver, $J_{Tr,max}$	15 km/s
Global surface mapping swarm	Maximum # moon encounters, $N_{1,max}$	5
	Maximum # spacecraft each encounters, $N_{2,max}$	5
	Maximum orientation velocity change, $\Delta v_{PC,max}$	1 km/s

Swarm Optimization. The iterative variation of the least $J_{Sw,map}$ among all optimization trials of Equation 33 is presented in Figure 13. It can be seen here, that the initial iterations show a large variation among all design trials, and consequently have large standard deviations. This transience indicates iterations that had no feasible solutions as at least one constraint was violated. In this case, the solvers computed their penalties, as described in Equation 37, and Deb, 2000. The performance metrics of all optimizer trials are presented in Table 9. In swarm optimization trials, each iteration of the GA solver ran for an average of about 39 s, while each PSO iteration recorded an average of 46 s. Additionally, as seen from Figure 13, all GA trials converged to a minimum of $N_{SW,map} = 3$ spacecraft, While a lowest value of $N_{Sw} = 4$ spacecraft was noted from all PSO trials. Due to the minimum size, the final solution selected was noted from the GA trials and is analyzed in the following sections.

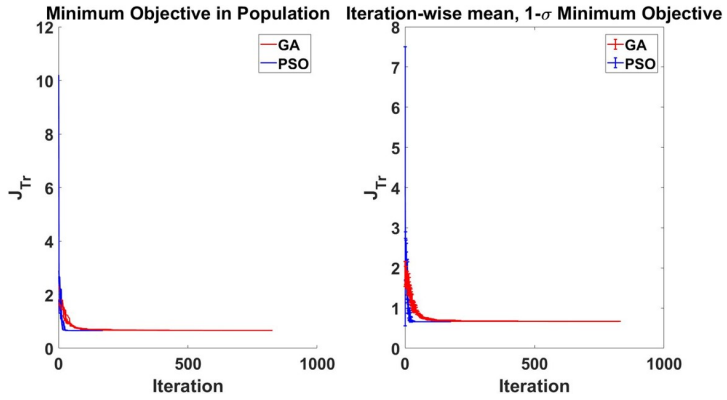

Figure 12: Variation of minimum objective in the trajectory design of the global surface mapping mission showing: the results of individual optimizer trials (left), and iteration-wise distribution of the two solvers (right)

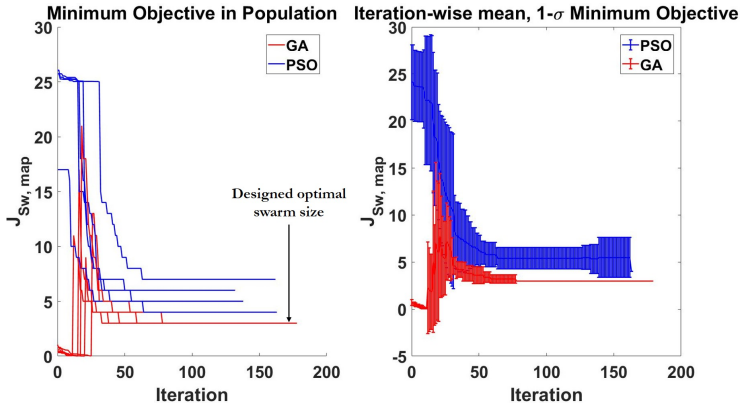

Figure 13: Variation of minimum objective in the swarm design of the global surface mapping mission showing: the results of individual optimizer trials (left), and iteration-wise distribution of the two solvers (right)

Optimal Trajectory. The decision vector of the selected optimal trajectory is presented in Table 10. As seen here, the all design variables are shown to satisfy the bounds noted in Table 8. The $C_{3,E}$ of the selected trajectory is 19.0 km^2/s^2, and has a $TF = 200$ days. The selected trajectory is presented in Figure 14. The contours presented in the porkchop plot (Vallado, 2013) in Figure 14, correspond to the bounds defined in Table 8. At the end of the heliocentric cruise, the computed excess velocity at arrival was $v_{\infty,2} = 2.47$ km/s. As shown in Table 10, the selected optimal resonance is $4 : 9$ resonance with $h_{p,min} = 327$ km from the surface of Mars. As described above, the design noted a value of $\Delta v_{OI,max} = 0.664$ km/s for its worst case orbit insertion maneuver.

Table 9: Time statistics of optimization solvers in case of the global surface mapping swarm mission.

Design Problem	Parameter	Solver	
		Genetic Algorithm	Particle Swarm Optimization
Trajectory	# solver trials	5	5
	Min, max execution time (s)	[72, 184]	[31, 56]
	Min, max # iterations	[355, 829]	[151, 172]
	Mean $\pm$ 1 $-$ σ execution time/iteration (s)	0.203 ± 0.01	0.227 ± 0.05
	Identified lowest objective (km/s)	0.664	0.659
Swarm	# solver trials	5	5
	Min, max execution time (hr)	[1.42, 1.91]	[1.45, 2.88]
	Min, max # iterations	[135, 180]	[127, 164]
	Mean $\pm$ 1 $-$ σ execution time/iteration (s)	38.7 ± 5	45.6 ± 10
	Identified lowest objective (# spacecraft)	3	4

Table 10: Decision vector of the optimal trajectory for the global surface mapping mission.

Parameter	Value
D_L	08/12/20, 14:20 hr
D_A	02/28/21, 10:09 hr
$h_{p,0}$	315 km
e_0	0.949
p	4
q	9

Optimal Swarm. The decision vector of the selected optimal swarm is presented in Table 11. The designed swarm contains $N_{Sw,map} = 3$ spacecraft which encounter the moon in two different locations. The configuration of the co-orbits of the spacecraft in the swarm along with the direction of the ${}^{N}\bar{V}^{-}_{\infty,2}$ is presented in Figure 15. The locations of the two encounters on the orbit of Deimos are shown here. The value of $\max(\Delta v_{OC,i})$ was noted as 0.95 km/s for the designed swarm co-orbits.

Table 11: Decision vector of the optimal swarm for the global surface mapping mission.

Parameter		Value
N_v		2
$N_{v,j}$		[2, 1]
$f_{v,j}$ (deg)		[6.6, 225]
$(\theta_{x,i}, \theta_{y,i})$ (deg)	Encounter-1	(226, -12.2)
		(144, 39)
	Encounter-2	(278, -8.2)

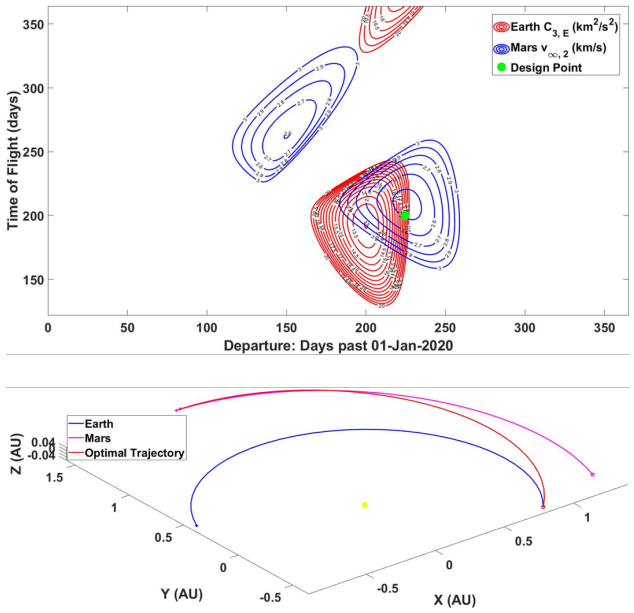

Figure 14: The selected optimal trajectory design with its mission parameters on Earth-Mars porkchop plot (top), and the corresponding interplanetary trajectory (bottom)

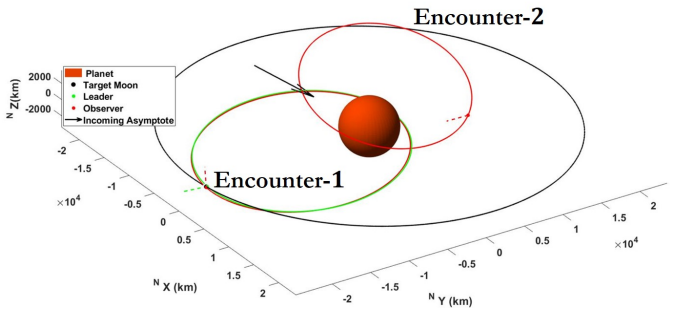

Figure 15: Configuration of the resonant co-orbits in the designed global surface mapping swarm.

Surface Coverage. The first encounter of the swarm, where 2 spacecraft encounter Deimos is shown in Figure 16, along with their instantaneous coverage. The variation of cumulative and instantaneous coverage over the orbital period of Deimos is presented in Figure 17. As seen here, at each encounter the instantaneous coverage is about 35 %. After the two encounters, we note a cumulative surface coverage of 90.5 % thus meeting the coverage requirement of the mission. The orthographic projections of the shape model of Deimos showing the cumulative coverage pattern after all encounters is shown in Figure 18.

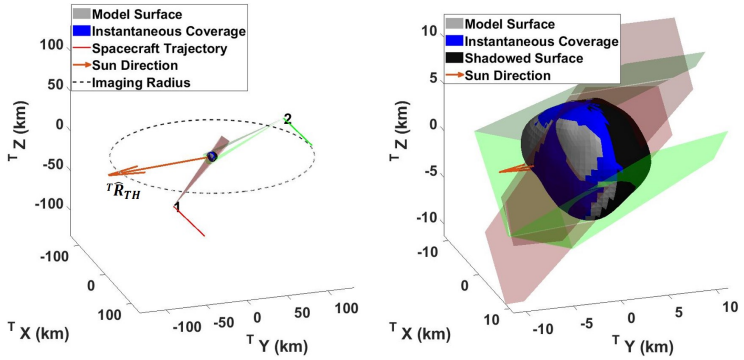

Figure 16: Encounter 1 of the swarm with Deimos, showing the spacecraft arrangement(left), and their instantaneous surface coverage pattern (right).

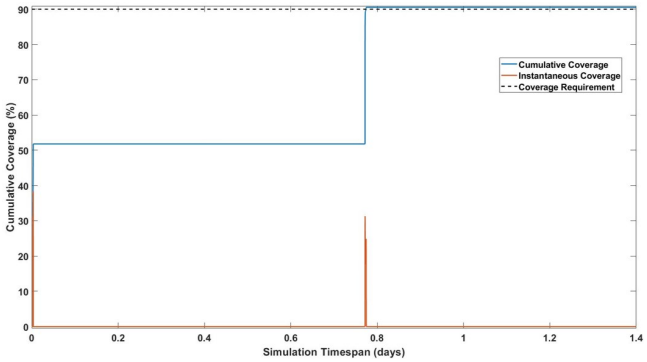

Figure 17: Time evolution of surface coverage of Deimos noted from spacecraft encounters.

Spacecraft Design. The Δv_{net} noted from substituting the Δv of the two maneuvers in Equation 29 was 2.1 km/s. The corresponding fuel mass required for the spacecraft in Appendix A was noted using rocket equation (Vallado, 2013) as 31 kg. The design parameters and seed spacecraft cost are presented in Table 12, where the costs are inflated to the launch year 2020 currency.

5.3. RoI Observation

The input parameters required for defining the trajectory and swarm in case of the RoI observation mission are presented in Table 13. The results of the trajectory and swarm optimization are as follows:

Trajectory Optimization. The variation of the least value of J_{Tr} noted from all optimization trials of Equation 32 is presented in Figure 19. Since the optimization problem is the same for the global surface mapping and RoI observation missions, the optimizer performances are nearly identical.The lowest value of $\Delta v_{OI,max}$, was noted as 0.667 km/s across all GA design simulations, while it was 0.659 km/s across all PSO simulations.

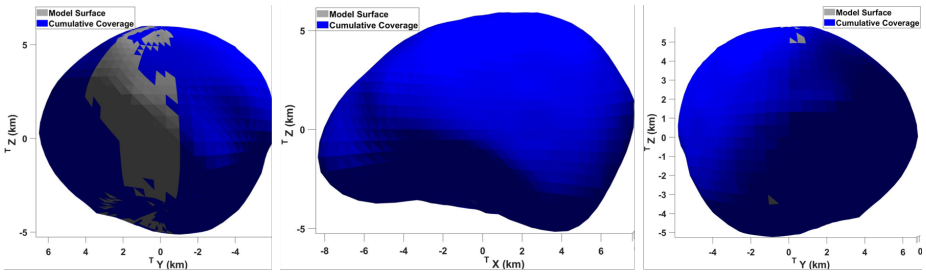

Figure 18: Cumulative coverage generated after all encounters of the swarm.

Table 12: Design and cost parameters corresponding to the global surface mapping mission.

Parameter	Value
Spacecraft fuel mass	**31.0 kg**
Spacecraft wet mass	**49.9 kg**
Spacecraft mission cost	**18.2 ± 1.1 LY$M**
Spacecraft launch cost	**0.98 ± 0.29 LY$M**

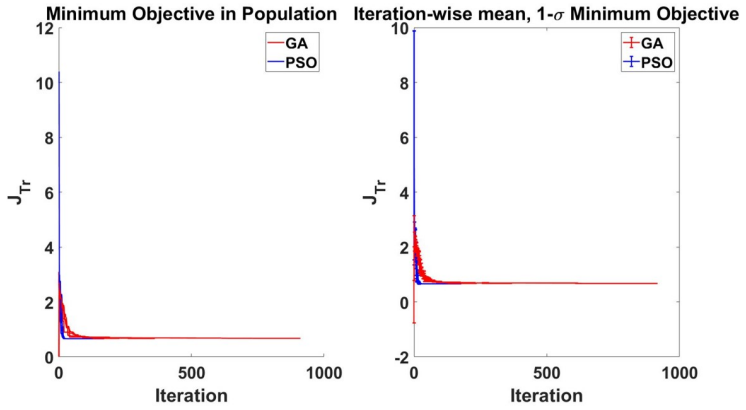

Figure 19: Variation of minimum objective in the trajectory design of the RoI observation mission showing: the results of individual optimizer trials (left), and iteration-wise distribution of the two solvers (right)

Swarm Optimization. The variation of the least $J_{Sw,map}$ among all optimization trials of Equation 34 is presented in Figure 20. The large initial transient variations in the optimizer trials are also attributed to the lack of feasible designs in the initial populations. The performance metrics of the swarm design can be noted from Table 14. As seen here, the mean execution time was noted to be nearly equal for both GA and PSO iterations. However, the PSO solver trials identified the final solutions in fewer trials, leading to shorter execution

Table 13: Trajectory and swarm definition parameters used in RoI Observation mission design.

Design Problem	Parameter	Value
Trajectory	Maximum launch energy, $C_{3,max,R}$	20 km^2/s^2
	Maximum time of flight, $TF_{max,R}$	200 days
	Maximum excess velocity at arrival, $v_{\infty,2,max,R}$	3 km/s
	Minimum Periapsis altitude, $h_{p,min,R}$	300 km
	Launch epoch bounds, $[D_{L,min}, D_{L,max}]$	[1/1/20, 00: 00 hr, 12/31/20, 00: 00 hr]
	Arrival epoch bounds, $[D_{A,min}, D_{A,max}]$	[5/1/20, 00: 00 hr, 12/31/21, 00: 00 hr]
	Maximum HEO eccentricity, $e_{1,max}$	0.98
	Resonance bounds, $[p_{min}, p_{max}]$	[1, 10]
	Resonance bounds, $[q_{min}, q_{max}]$	[1, 20]
	Maximum objective for PSO solver, $J_{Tr,max}$	15 km/s
RoI observation swarm	Maximum # moon encounters, $N_{1,max}$	15
	Maximum orientation velocity change, $\Delta v_{PC,max}$	2 km/s

times. Both solvers recorded a minimum value of $N_{Sw,RoI} = 4$ spacecraft. The selected design corresponded to a 4 spacecraft swarm identified by the GA solver with the least value of $\Delta v_{OI,max}$ as 0.667 km/s, as the PSO trial with the least $\Delta v_{OI,max}$, the swarm optimization solution converged to a 5 spacecraft swarm.

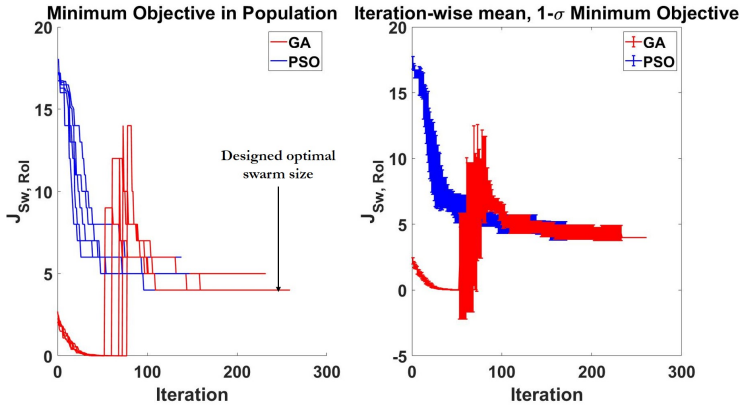

Figure 20: Variation of minimum objective in the swarm design of the RoI observation mission showing: the results of individual optimizer trials (left), and iteration-wise distribution of the two solvers (right)

Optimal Trajectory. The decision vector of the selected optimal trajectory is presented in Table 15. As seen here, the D_L, and D_A epochs are with in one day of the epochs noted in Table 10. As a result, the trajectory is identical to Figure 14. The $C_{3,E}$, TF, and $v_{\infty,2}$ of the selected trajectory are 19.0 km^2/s^2, 200 days, and 2.47 km/s respectively. As shown in Table 15, the selected optimal

Table 14: Time statistics of optimization solvers in case of the RoI observation swarm mission.

Design Problem	Parameter	Solver	
		Genetic Algorithm	Particle Swarm Optimization
Trajectory	# solver trials	5	5
	Min, max execution time (s)	[49, 222]	[29, 37]
	Min, max # iterations	[231, 913]	[141, 172]
	Mean $\pm$ 1 $-$ σ execution time/iteration (s)	0.230 ± 0.01	0.212 ± 0.01
	Identified lowest objective (km/s)	0.667	0.659
Swarm	# solver trials	5	5
	Min, max execution time (hr)	[7.4, 20.3]	[5.62, 25.4]
	Min, max # iterations	[203, 261]	[139, 196]
	Mean $\pm$ 1 $-$ σ execution time/iteration (s)	264 ± 81	264 ± 175
	Identified lowest objective (# spacecraft)	4	4

resonance is also a $4:9$ resonance.

Table 15: Decision vector of the optimal trajectory for the RoI observation mission.

Parameter	Value
D_L	08/13/20, 13:29 hr
D_A	02/28/21, 17:57 hr
$h_{p,0}$	377 km
e_0	0.978
p	4
q	9

Optimal Swarm. The decision vector of the selected optimal swarm is presented in Table 16. The designed swarm contains $N_{Sw,map} = 4$ spacecraft which serially encounter Deimos at 4 separate locations listed in Table 16. The configuration of the resonant co-orbits of the spacecraft in the swarm along with the direction of the ${}^{N}\bar{V}^{-}_{\infty,2}$ is presented in Figure 21. The value of $\max(\Delta v_{OC,i})$ was noted as 1.81 km/s for the designed swarm co-orbits.

Table 16: Decision vector of the optimal swarm for the global surface mapping mission.

Parameter		Value
N_v		4
$f_{v,j}$ (deg)		[202, 208, 211, 212]
($\theta_{x,i}$, $\theta_{y,i}$) (deg)	Encounter-1	(222, 7.1)
	Encounter-2	(219, 11.0)
	Encounter-3	(218, 19.7)
	Encounter-4	(221, 25.8)

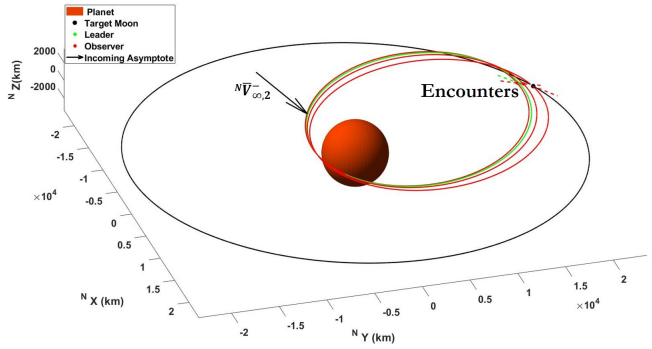

Figure 21: Configuration of the resonant co-orbits in the designed RoI observation swarm.

RoI Coverage. The first encounter in the swarm, where a single spacecraft observes the selected RoI is shown in Figure 22. The variation of spatial and temporal RoI coverage over the simulation time span is presented in Figure 23.

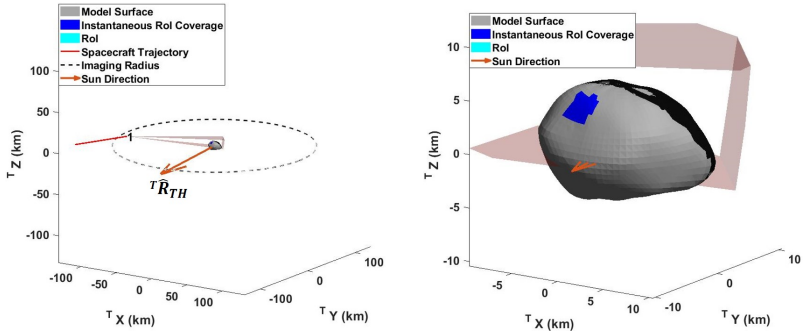

Figure 22: Encounter 1 of the swarm with Deimos, showing a spacecraft location (left), and its instantaneous RoI coverage pattern (right).

As seen here, after 4 encounters with Deimos, the spacecraft can achieve a 100 % surface coverage of the RoI while observing it for a total of 20.7 mins. Furthermore, while coverage continuity (Wertz, Everett, and Puschell, 2011) was not designed in the current work, all 4 encounters occur near the same true anomaly of Deimos as noted from Table 16, which allows a nearly continuous coverage as seen in Figure 17. The RoI surface covered after all spacecraft flybys is presented in Figure 24, where all faces in the RoI are noted to be observed.

Spacecraft Design. The total Δv_{net} noted from Equation 29 was 3.22 km/s for The RoI. The fuel mass, and individual cost associated with the seed spacecraft are presented in Table 12. The costs described here are also inflated in the launch year 2020 currency as noted from Table 15.

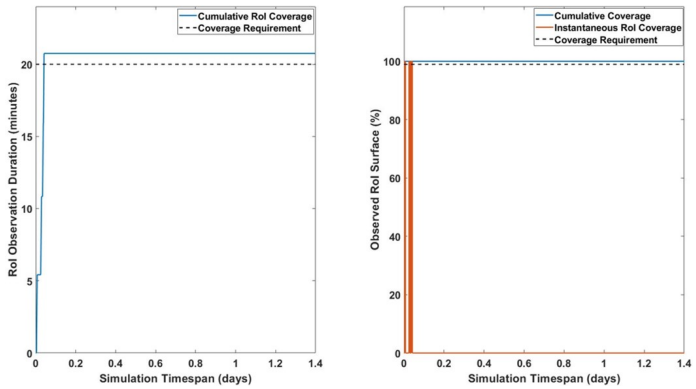

Figure 23: Time evolution of surface coverage of Deimos noted from spacecraft encounters.

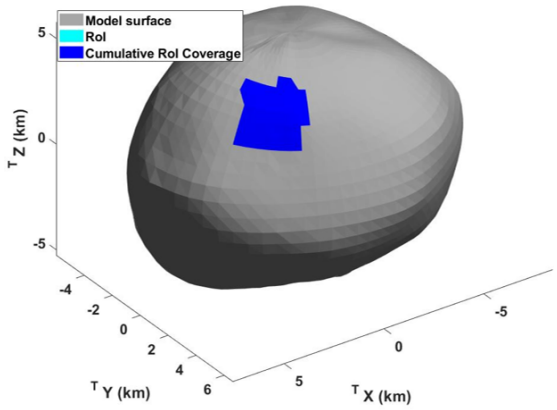

Figure 24: Cumulative RoI coverage after all encounters of the swarm.

5.4. Swarm Mission Costs

The estimated space-segment costs for the two missions, noted from Equations 30 and 31 are presented in Table 18. The costs are inflated to their launch year 2020. As noted here, the global surface mapping mission has an estimated space segment cost of 53.4 ± 2 LY$M if built from 3 seed spacecraft presented in Table 12. The RoI observation mission has an estimated space segment cost of 75 ± 2.5 LY$M if built from 4 seed spacecraft presented in Table 17. However, as mentioned above, while the accuracy of the cost estimation is limited, it can help identify a ballpark estimate in the initial mission design phase.

5.5. Discussion

The results in the current work provide key insights into spacecraft swarms applications and their mission design. The current work suggests that spacecraft flybys can overcome the spatial and temporal coverage limitations of single

Table 17: Design and cost parameters corresponding to the RoI observation mission.

Parameter	Value
Spacecraft fuel mass	65.3 kg
Spacecraft wet mass	84.1 kg
Spacecraft mission cost	19.1 ± 1.1 LY$M
Spacecraft launch cost	1.66 ± 0.49 LY$M

Table 18: Estimated space segment costs associated with the two swarm missions

Parameter	Global Surface Mapping	RoI Observation
Mission cost	50.4 ± 2.0 LY$M	68.9 ± 2.3 LY$M
Launch cost	2.95 ± 0.5 LY$M	6.63 ± 1.0 LY$M
Total space segment cost	53.4 ± 2.0 LY$M	75.6 ± 2.5 LY$M

spacecraft flybys, which is valuable for exploring small bodies such as planetary moons. Second, the current work described a mission design software where the interplanetary trajectory, swarm operations, and the seed spacecraft designs are carried out in the same environment. The key advantage of such a design tool over traditional tools that perform stand-alone design optimization is that a common environment can identify incompatible solutions, and also reduce the need for design duplication thus accelerating the mission design process. However, we acknowledge that spacecraft swarm mission design is highly interconnected. Even in the case of simplified mission architectures used in the current work, the spacecraft payload influenced the trajectory, and encounter design points for the swarms, which in turn influenced the fuel cost corresponding to the orbit insertion maneuver. Therefore, a practical mission design tool must allow for design iterations. Since the focus of the current work was on the Automated Swarm Designer module, we presented a single execution of the swarm design optimization, while showing its interaction with the trajectory and spacecraft designs. Furthermore, this suggests that overall mission requirements such as total cost, fuel, and weight requirements can be used in the future development of IDEAS to allow design iterations using the Mission Analyzer module. The key contributions of the current work to the existing state-of-the-art in the field of space mission design research are summarized as follows. First, the current work proposed novel spacecraft swarm missions to study small, irregular planetary moons. The spacecraft are deployed on resonant co-orbits that encounter the moon near their apoapsis. Next, we formulated the trajectory and swarm design optimization of these co-orbits for missions with space-based and time-based applications. The optimization problems are solved using two evolutionary algorithms, which are programmed into the corresponding design modules of IDEAS. Finally, we demonstrated the algorithms in the current work through numerical simulations, while presenting the interactions between different design modules in IDEAS.

6. Conclusion

The current work presented mission design algorithms to explore irregular planetary moons using flybys of spacecraft swarms. The swarms will be deployed on co-orbits around the central planet, while periodically exploring the moon at their apoapsis. The application of these co-orbits to space-based and time-based visual mapping missions is presented. The algorithms presented are programmed into the IDEAS software, which as an end-to-end tool for spacecraft swarm mission design. We began by defining the coverage requirements for global surface mapping mission, as an example of a spatial coverage application, and RoI observation mission for temporal coverage applications We then presented the models of the two missions, where the swarm, trajectory, and spacecraft design parameters were identified. The parameters were used to formulate the swarm and trajectory design optimization problems, and their solution methodology using different optimization solvers was discussed. We then presented case studies where the two visual mapping swarm missions were designed to explore the surface of Deimos while demonstrating the interactions between the different design modules of IDEAS. While the current work presented applications of the Automated Swarm Designer module to design Class 2 swarm missions to explore planetary moons, few simplifying assumptions were made in modeling the missions. To improve the fidelity of the design, future work on IDEAS will focus on iterative mission design using the Mission Analyzer module, while exploring more swarm architectures. Additionally, future work will also focus on building the spacecraft subsystem inventory and the Automated Spacecraft Designer module. Finally, while in the current work we only considered two-body dynamics, future work will focus on trajectory design in high fidelity dynamical environments. This will be useful in planning additional correction maneuvers, which increases the accuracy of spacecraft mass, and mission cost estimation. These augmentations will improve the quality of solutions from IDEAS, thus providing a powerful tool to develop holistically optimal missions for small body exploration.

Appendix A. Seed Spacecraft Dry Mass

In this section, we list the subsystems of the seed spacecraft used for fuel mass and cost estimation. The subsystem list mentioned here was obtained by surveying existing off-the-shelf small spacecraft hardware. However, it is explicitly stated here that the feasibility of building such a seed spacecraft is not considered in the current work. The subsystems are listed as follows:

Payload. The camera payload of the CubeSat mission Asteria (Pong, Lim, M. W. Smith, et al., 2010) was used as the baseline of the seed spacecraft camera model considered in the current work. The camera has an aperture diameter of $D_c = 8$ cm, and is assumed to weigh a total of 0.57 kg, and has a power consumption of 2 W. To compute payload cost, we conservatively assume that the camera has a design life of 4 yrs.

Attitude Control System. The XACT-50 module developed by Blue Canyon Technologies, Inc., is selected as the baseline attitude determination and control system (ADCS) for the seed spacecraft which has an estimated mass of 1.23 kg.

Communications. The IRIS V2.1 developed by the Jet Propulsion Laboratory (Kobayashi, Holmes, Yarlagadda, et al., 2019) is assumed as the baseline communication system for the seed spacecraft and has an estimated weight of 1.2 kg.

Command and Data Handling. the CubeSat Processor (CSP) by Space Micro Inc. is assumed to be the command and data handling module (CDH) which has an estimated mass of 60 g.

Power. The seed spacecraft is assumed to have a CubeSat grade Lithium battery manufactured by Pumpkin Space Inc., which weighs about 0.71 kg. In addition, we assume that the spacecraft uses a power distribution board from the same vendor which weighs a total of 0.155 kg, and MMA Hawk solar panels with a mass of 0.558 kg. Therefore, the power system is estimated to weigh a total of 1.42 kg.

Structure and Thermal. Since the seed spacecraft described here is assumed to belong to small spacecraft class (Wertz, Everett, and Puschell, 2011), we conservatively assume a net supporting structural mass of 10 kg, and an additional 2 kg mass for thermal protection.

Propulsion. The MPS-120XL system from Aerojet Rocketdyne Holdings Inc is assumed to be the baseline propulsion subsystem of the seed spacecraft. This propulsion system has a dry mass of 2.4 kg. We assume that the fuel used is hydrazine with a specific impulse of 220 s (Vallado, 2013). The fuel mass is estimated such that the spacecraft can perform the worst case orbit insertion and orientation change maneuvers as described by Equation 29. The resulting mass distribution of the spacecraft is summarized in Table A.19.

Table A.19: Mass distribution of the seed spacecraft obtained by a collection of existing off-the-shelf equipment.

Parameter	Mass (kg)
Payload	**0.57**
ADCS	**1.23**
Communication	**1.2**
CDH	**0.06**
Power	**1.42**
Structure	**10**
Thermal	**2**
Propulsion dry mass	2.4
Total dry mass	**18.9**

References

Aleshkina, E. Y. (2009). "Synchronous spin-orbital resonance locking of large planetary satellites". In: *Solar System Research* 43.1, pp. 71–78.

Balázs, A. (2018). "A Comet Revisited: Lessons Learned from Philaes Landing". In: *IEEE Software* 35.4, pp. 89–93.

Bandyopadhyay, S., Foust, R., Subramanian, G. P., Chung, S., and Hadaegh, F. Y. (2016). "Review of formation flying and constellation missions using nanosatellites". In: *Journal of Spacecraft and Rockets* 53.3, pp. 567–578.

Buffington, B. (2014). "Trajectory Design Concept for the Proposed Europa Clipper Mission". In: *AIAA/AAS Astrodynamics Specialist Conference*, p. 4105.

Campagnola, S., Yam, C. H., Tsuda, Y., Ogawa, N., and Kawakatsu, Y. (2018). "Mission analysis for the Martian Moons Explorer (MMX) mission". In: *Acta Astronautica* 146, pp. 409–417.

Castillo-Rogez, J. C., Pavone, M., Hoffman, J. A., and Nesnas, I. A. (2012). "Expected science return of spatially-extended in-situ exploration at small solar system bodies". In: *2012 IEEE Aerospace Conference*. IEEE, pp. 1–15.

Conn, T., Perez, A., Plice, L., and Ho, M. (2017). "Operating Small Sat Swarms as a Single Entity: Introducing SODA". In: *31st Annual AIAA/USU conference on Small Satellites*, pp. 1–9.

Conte, D. (2014). "Determination of Optimal Earth-Mars Trajectories to Target the Moons of Mars". PhD thesis. The Pennsylvania State University.

Deb, K. (2000). "An efficient constraint handling method for genetic algorithms". In: *Computer methods in applied mechanics and engineering* 186.2-4, pp. 311–338.

Deep, K., Singh, K. P., Kansal, M. L., and Mohan, C. (2009). "A real coded genetic algorithm for solving integer and mixed integer optimization problems". In: *Applied Mathematics and Computation* 212.2, pp. 505–518.

Duxbury, T. C., Zakharov, A., Hoffmann, H., and Guinness, E. (2014). "Spacecraft exploration of Phobos and Deimos". In: *Planetary and Space Science* 102, pp. 9–17.

Galvez, A., Carnelli, I., Michel, P., Cheng, A., Reed, C., Ulamec, S., Biele, J., Zbrll, P., and Landis, R. (2013). "AIDA: The asteroid impact and deflection assessment mission". In: *European Planetary Science Congress*. Vol. 8, EPSC2013–1043.

Giorgini, J. D. (2015). "Status of the JPL horizons ephemeris system". In: *IAU General Assembly* 22.

Goldman, R. N. (1991). "Area of planar polygons and volume of polyhedra". In: *Graphics gems II*. Elsevier, pp. 170–171.

Gooding, R. (1990). "A procedure for the solution of Lambert's orbital boundary-value problem". In: *Celestial Mechanics and Dynamical Astronomy* 48.2, pp. 145–165.

Grasset, O., Dougherty, M., Coustenis, A., Bunce, E., Erd, C., Titov, D., Blanc, M., Coates, A., Drossart, P., Fletcher, L., et al. (2013). "JUpiter ICy moons Explorer (JUICE): An ESA mission to orbit Ganymede and to characterise the Jupiter system". In: *Planetary and Space Science* 78, pp. 1–21.

Grewal, M. S., Weill, L. R., and Andrews, A. P. (2007). *Global positioning systems, inertial navigation, and integration*. John Wiley & Sons, Hoboken, NJ.

Habib-Agahi, H., Ball, G., and Fox, G. (2009). "NICM Schedule and Cost Rules of Thumb". In: *AIAA SPACE 2009 Conference & Exposition*, p. 6512.

Hanselman, D. C. and Littlefield, B. (2005). *Mastering matlab 7*. Pearson/Prentice Hall, Upper Saddle River, NJ.

Hartmann, J. W., Coverstone, V., and Williams, S. N. (1998). "Optimal interplanetary spacecraft trajectories via a Pareto genetic algorithm". In: *Journal of the Astronautical Sciences* 46.3, pp. 267–282.

Kennedy, J. and Eberhart, R. (1995). "Particle swarm optimization". In: *Proceedings of ICNN'95-International Conference on Neural Networks*. Vol. 4. IEEE, pp. 1942–1948.

Kobayashi, M. M., Holmes, S., Yarlagadda, A., Aguirre, F., Chase, M., Angkasa, K., Burgett, B., McNally, L., Dobreva, T., and Satorius, E. (2019). "The Iris Deep-Space Transponder for the SLS EM-1 Secondary Payloads". In: *IEEE Aerospace and Electronic Systems Magazine* 34.9, pp. 34–44.

Lohn, J. D., Linden, D. S., Hornby, G. S., and Kraus, W. F. (2004). "Evolutionary design of an X-band antenna for NASA's space technology 5 mission". In: *IEEE Antennas and Propagation Society Symposium, 2004.* Vol. 3. IEEE, pp. 2313–2316.

Mahr, E., Tu, A., and Gupta, A. (2016). "Development of the small satellite cost model 2014 (SSCM14)". In: *2016 IEEE Aerospace Conference*. IEEE, pp. 1–13.

Marghitu, D. B. and Dupac, M. (2012). "Vector Algebra". In: *Advanced Dynamics*. Springer, pp. 1–71.

Mortari, D., Wilkins, M. P., and Bruccoleri, C. (2004). "The flower constellations". In: *Journal of Astronautical Sciences* 52.1, pp. 107–127.

Murray, C. D. and Dermott, S. F. (1999). *Solar system dynamics*. Cambridge university press, Cambridge, NY.

Nallapu, R. and Thangavelautham, J. (2019a). "Attitude Control of Spacecraft Swarms for Visual Mapping of Planetary Bodies". In: *2019 IEEE Aerospace Conference*, pp. 1–16.

— (2019b). "Cooperative Multi-spacecraft Observation of Incoming Space Threats". In: *2019 Advanced Maui Optical Science (AMOS) Proceedings*. AMOS Tech., pp. 1–14.

— (2019c). "Spacecraft Swarm Attitude Control for Small Body Surface Observation". In: *2019 Advances in the Astronautical Sciences(AAS)-GNC Conference Proceedings*. AAS-GNC, pp. 1–12.

— (2019d). "Towards End-To-End Design of Spacecraft Swarms for Small-Body Reconnaissance". In: *Proceedings of the International Astronautical Congress, IAC*. International Astronautical Federation, IAF, p. 1.

— (2020). "Design of Spacecraft Swarm Flybys for Planetary Moon Exploration". In: *AIAA Scitech 2020 Forum*, p. 0954.

Nallapu, R., Thoesen, A., Garvie, L., Asphaug, E., and Thangavelautham, J. (2016). "Optimized Bucket Wheel Design for Asteroid Excavation". In: *Pro-*

ceedings of the International Astronautical Congress, IAC. International Astronautical Federation, IAF, p. 34715.

Nallapu, R., Vance, L., Xu, Y., and Thangavelautham, J. (2020). "Automated Design Architecture for Lunar Constellations". In: *2020 IEEE Aerospace Conference Proceedings*. IEEE, p. 1.

Nallapu, R., Xu, Y., Marquez, A., Schuler, T., and Thangavelautham, J. (2020). "The Design of a Space-Based Observation and Tracking System For Interstellar Objects". In: *2020 Advances in the Astronautical Sciences(AAS)-GNC Conference Proceedings*. AAS-GNC, p. 1.

Phillips, C. B. and Pappalardo, R. T. (2014). "Europa Clipper mission concept: exploring Jupiter's ocean moon". In: *Eos, Transactions American Geophysical Union* 95.20, pp. 165–167.

Pong, C. M., Lim, S., Smith, M. W., Miller, D. W., Villaseñor, J. S., and Seager, S. (2010). "Achieving high-precision pointing on ExoplanetSat: initial feasibility analysis". In: *Space Telescopes and Instrumentation 2010: Optical, Infrared, and Millimeter Wave*. Vol. 7731. International Society for Optics and Photonics, p. 77311V.

Rao, S. S. (2019). *Engineering optimization: theory and practice*. John Wiley & Sons, Hoboken, NJ.

Schaub, H. and Junkins, J. L. (2013). *Analytical mechanics of space systems*. American Institute of Aeronautics and Astronautics, Reston, VA.

Scheeres, D. J. (2016). *Orbital motion in strongly perturbed environments: applications to asteroid, comet and planetary satellite orbiters*. Springer Berlin Heidelberg, Berlin, Heidelberg.

Schoolcraft, J., Klesh, A. T., and Werne, T. (2016). "MarCO: interplanetary mission development on a CubeSat scale". In: *14th International Conference on Space Operations*, p. 2491.

Smith Jr, J. C. and Bell, J. L. (2005). "2001 Mars Odyssey Aerobraking". In: *Journal of spacecraft and rockets* 42.3, pp. 406–415.

Sobel, I. (1972). *Camera models and machine perception*. Tech. rep. Computer Science Department, Technion.

Spencer, D. A. and Tolson, R. (2007). "Aerobraking cost and risk decisions". In: *Journal of Spacecraft and Rockets* 44.6, pp. 1285–1293.

Thomas, P., Yoder, C., Synnott, S., Salo, H., Veverka, J., Simonelli, D., Helfenstein, P., Carcich, B., Black, G., Nicholson, P., et al. (2000). "Small Body Shape Models V2. 1". In: *NASA Planetary Data System* 173.

Tsiotras, P., Shen, H., and Hall, C. (2001). "Satellite attitude control and power tracking with energy/momentum wheels". In: *Journal of Guidance, Control, and Dynamics* 24.1, pp. 23–34.

Vallado, D. A. (2013). *Fundamentals of Astrodynamics and Applications*. Microcosm Press, Hawthorne, CA.

Wallace, M., Parker, J., Strange, N., and Grebow, D. (2012). "Orbital operations for Phobos and Deimos exploration". In: *AIAA/AAS Astrodynamics Specialist Conference*, p. 5067.

Wertz, J. R., Everett, D. F., and Puschell, J. J. (2011). *Space mission engineering: the new SMAD*. Microcosm Press, Hawthorne, CA.

Weston, S., Miller, C. S., Ingersoll, J. E., Yost, B. D., Agasid, E., Burton, R., Carlino, R., Defouw, G., Perez, A. D., Karacalioglu, A. G., et al. (2018). *State of the Art: Small Spacecraft Technology*. Tech. rep. NASA.

Zamaro, M. and Biggs, J. D. (2016). "Identification of new orbits to enable future mission opportunities for the human exploration of the Martian moon Phobos". In: *Acta Astronautica* 119, pp. 160–182.

Zuber, M. T., Smith, D. E., Watkins, M. M., Asmar, S. W., Konopliv, A. S., Lemoine, F. G., Melosh, H. J., Neumann, G. A., Phillips, R. J., Solomon, S. C., et al. (2013). "Gravity field of the Moon from the Gravity Recovery and Interior Laboratory (GRAIL) mission". In: *Science* 339.6120, pp. 668–671.